

## Atomic Shocks in the Outflow of L1551 IRS 5 Identified with SOFIA-upGREAT Observations of [O I]

YAO-LUN YANG,<sup>1</sup> NEAL J. EVANS II,<sup>2</sup> AGATA KARSKA,<sup>3</sup> LARS E. KRISTENSEN,<sup>4</sup> REBECA ALADRO,<sup>5</sup> JON P. RAMSEY,<sup>1</sup>  
JOEL D. GREEN,<sup>6,2</sup> AND JEONG-EUN LEE<sup>7</sup>

<sup>1</sup>*Department of Astronomy, University of Virginia, Charlottesville, VA 22904, USA*

<sup>2</sup>*Department of Astronomy, The University of Texas at Austin, Austin, TX 78712, USA*

<sup>3</sup>*Institute of Astronomy, Faculty of Physics, Astronomy and Informatics, Nicolaus Copernicus University, Grudziadzka 5, 87-100 Torun, Poland*

<sup>4</sup>*Niels Bohr Institute & Centre for Star and Planet Formation, Copenhagen University, Øster Voldgade 5-7, 1350 Copenhagen K, Denmark*

<sup>5</sup>*Max-Planck-Institut für Radioastronomie, Auf dem Hügel 69, D-53121 Bonn, Germany*

<sup>6</sup>*Space Telescope Science Institute, Baltimore, MD 02138, USA*

<sup>7</sup>*Department of Astronomy & Space Science, Kyung Hee University, Gyeonggi 446-701, Korea  
School of Space Research, Kyung Hee University, Yongin-shi, Kyungki-do 449-701, Korea*

### ABSTRACT

We present velocity resolved SOFIA/upGREAT observations of [O I] and [C II] lines toward a Class I protostar, L1551 IRS 5, and its outflows. The SOFIA observations detect [O I] emission toward only the protostar and [C II] emission toward the protostar and the red-shifted outflow. The [O I] emission has a width of  $\sim 100$  km s<sup>-1</sup> only in the blue-shifted velocity, suggesting an origin in shocked gas. The [C II] lines are narrow, consistent with an origin in a photodissociation region. Differential dust extinction from the envelope due to the inclination of the outflows is the most likely cause of the missing red-shifted [O I] emission. Fitting the [O I] line profile with two Gaussian components, we find one component at the source velocity with a width of  $\sim 20$  km s<sup>-1</sup> and another extremely broad component at  $-30$  km s<sup>-1</sup> with a width of  $87.5$  km s<sup>-1</sup>, the latter of which has not been seen in L1551 IRS 5. The kinematics of these two components resemble cavity shocks in molecular outflows and spot shocks in jets. Radiative transfer calculations of the [O I], high- $J$  CO, and H<sub>2</sub>O lines in the cavity shocks indicate that [O I] dominates the oxygen budget, making up more than 70% of the total gaseous oxygen abundance and suggesting [O]/[H] of  $\sim 1.5 \times 10^{-4}$ . Attributing the extremely broad [O I] component to atomic winds, we estimate the intrinsic mass loss rate of  $(1.3 \pm 0.8) \times 10^{-6} M_{\odot} \text{ yr}^{-1}$ . The intrinsic mass loss rates derived from low- $J$  CO, [O I], and HI are similar, supporting the model of momentum-conserving outflows, where the atomic wind carries most momentum and drives the molecular outflows.

### 1. INTRODUCTION

Protostellar outflows are the primary mechanism of angular momentum removal that facilitates the growth of protostars. Outflows also allow transportation of materials from the disk to the protostars, injecting kinetic energy into the surroundings. The outflow-envelope interaction can lead to UV-irradiated outflow cavities and shocks both along the outflows and on the cavity walls (e.g., Kristensen et al. 2012; Karska et al. 2014a; Yang et al. 2018). Atomic oxygen fine-structure lines are important cooling lines that trace shocked gas in outflows (e.g., Nisini et al. 2015; Karska et al. 2018), especially

the  $^3P_1 \rightarrow ^3P_2$  transition at  $63 \mu\text{m}$ . If the [O I] emission comes from dissociative J-shocks in the outflow, where [O I] dominates the cooling, the [O I] luminosity could trace the mass loss rate (Hollenbach 1985; Hollenbach & McKee 1989). Studies using observations of the Herschel Space Observatory surveyed the [O I]  $63 \mu\text{m}$  line from low-mass to high-mass protostars with many results suggesting that the line originates in UV-irradiated shocks (Karska et al. 2014b; Nisini et al. 2015; Karska et al. 2018). However, the velocity resolution of the Herschel instruments was not sufficient to resolve the line profile of [O I], although significant velocity offsets of the line centroid were seen in several outflows (van Kempen et al. 2010; Lee et al. 2014; Riviere-Marichalar et al. 2016).

With the advent of the Stratospheric Observatory for Infrared Astronomy (SOFIA), it became possible to ob-

tain velocity-resolved spectra of the [O I] line. In a massive star-forming region, Leurini et al. (2015) show complex line profiles of [O I] observed by SOFIA, including high-velocity line wings and absorption around the source velocity. Thus, a faithful representation of different components in the outflow requires velocity-resolved line profiles. Toward NGC 1333 IRAS 4A, a low-mass protostar, Kristensen et al. (2017a) used SOFIA to observe the [O I] 63  $\mu\text{m}$  line in the R1 shock knot along the outflow. The line profile of the [O I] emission is similar to that of CO  $J = 16 \rightarrow 15$  and shock-excited H<sub>2</sub>O lines, implying that they trace the same shock component. They suggest that CO is the major carrier of volatile oxygen in the shock and only  $\sim 15\%$  of the oxygen is atomic. Similar high-spectral-resolution observations of [O I] have been only performed in a few intermediate-mass (Gusdorf et al. 2017; Schneider et al. 2021) and high-mass protostars (Leurini et al. 2015; Schneider et al. 2018) due to the lower [O I] brightness in low-mass protostars.

L1551 IRS 5 has an exceptionally high [O I] 63  $\mu\text{m}$  luminosity among low-mass protostars (Green et al. 2016), making it an ideal target to study the kinematics and energetics of [O I] in low-mass protostars. L1551 IRS 5 is a Class I binary protostar (Rodríguez et al. 1998) at a distance of  $147.3 \pm 0.5$  pc (Galli et al. 2018). The two protostars are separated by  $\sim 50$  au ( $0''.3$ ) and each hosts its own disk with a radius of  $\sim 10$  au (Rodríguez et al. 1998; Lim & Takakuwa 2006; Lim et al. 2016), sharing a circumbinary disk (Cruz-Sáenz de Miera et al. 2019). Each source drives its own jet observed in free-free emission (Rodríguez et al. 2003) and the [Fe II] 1.644  $\mu\text{m}$  line (Pyo et al. 2005, 2009). The [Fe II] emission is only observed at blue-shifted velocities, extending  $\sim 10''$  to the southwest with a maximum velocity of  $-400$   $\text{km s}^{-1}$ . L1551 IRS 5 has molecular bipolar outflows in the northeast-southwest direction, first recognized by Snell et al. (1980) with CO, which is in fact the first discovery of molecular outflows in protostars. Wu et al. (2009) constrained a half outflow opening angle of  $22^\circ$  and a position angle of  $57^\circ$  using the CO  $J = 2 \rightarrow 1$  line observed by the Submillimeter Array. Chou et al. (2014) further constrained the disk inclination angle of  $60^\circ \pm 5^\circ$  with respect to the plane of sky by modeling the Keplerian circumbinary disk, suggesting an inclination of  $30^\circ$  for the outflow. Fridlund et al. (2002) derived a source velocity of  $6.5$   $\text{km s}^{-1}$  for L1551 IRS 5, while Yıldız et al. (2013) found a slightly lower source velocity of  $6.2$   $\text{km s}^{-1}$ , which has since been adopted by several studies of high- $J$  CO and water emission (e.g., Kristensen et al. 2017b). Thus, we adopt a source velocity  $6.2$   $\text{km s}^{-1}$  in this study to ensure consistent comparisons. Taken to-

gether, the long history of studies on L1551 IRS 5 make it one of the best-studied Class I outflows, and thus an ideal target for a more detailed study of [O I] emission in protostellar outflows.

In this study, we present velocity-resolved spectra of the [O I] 63  $\mu\text{m}$  and [C II] 158  $\mu\text{m}$  lines observed towards L1551 IRS 5 with SOFIA. Section 2 describes the observations and data reduction. Section 3 presents the spectra of [O I] and [C II] and compares the observations with archival Herschel data. Section 4 discusses the origin of the [O I] emission in L1551 IRS 5, how it related to shocks in the outflow, the oxygen budget in shocks, and the outflow mass loss rate inferred from the [O I] emission. Section 5 presents the conclusions of this study.

## 2. OBSERVATIONS

The observations of L1551 IRS 5 (Project ID: 06\_0104, PI: Y.-L. Yang) were conducted with SOFIA/upGREAT (upgrade German REceiver for Astronomy at Terahertz Frequencies; Risacher et al. 2016, 2018; Temi et al. 2018) in Cycle 6 (2018 December 5) and 7 (2020 March 5, 10, and 13) with aircraft altitudes ranging from 39,000 to 41,000 feet. Three positions toward L1551 IRS 5 were observed, including the central protostar as well as the known blue- and red-shifted outflows. The “blue” and “red” pointings are separated from the central protostar by  $6''.9$  along the outflow direction (PA= $57^\circ$ ; Wu et al. 2009).

We used multipixel receivers HFA (high frequency array) and LFA (low frequency array) connected to the Fast-Fourier-Transform spectrometer XFFTS. The LFA receiver consists of  $2 \times 7$  pixels for orthogonal polarizations in a hexagonal configuration with a central pixel, while the HFA has the same array geometry but only a single linear polarization. We configured the HFA to target the [O I]  $^3P_1 \rightarrow ^3P_2$  transition at 4.7447775 THz (63.18  $\mu\text{m}$ ) and the LFA to simultaneously observe the [C II]  $^2P_{3/2} \rightarrow ^2P_{1/2}$  transition at 1.9005369 THz (157.74  $\mu\text{m}$ ) and the OH doublet  $^2\Pi_{1/2, 3/2}^- \rightarrow ^2\Pi_{1/2, 1/2}^+$  transition at 1.8347598 and 1.83904685 THz (163.40 and 163.12  $\mu\text{m}$ ) in horizontal and vertical polarizations, respectively. No OH emission was detected in our observations, consistent with previous Herschel/PACS observations (Green et al. 2016), and thus, in this study, we focus on the [O I] and [C II] emission. The half-power beam widths (HPBW) of the HFA and LFA observations are  $6''.3$  and  $14''.1$ , respectively.

We rotated the arrays by  $-33^\circ$  to align the center row of three pixels in both HFA and LFA with the outflow direction. Henceforth, we refer to the positions toward the protostar, the red- and blue-shifted outflows as “center”,

“red”, and “blue” positions (Table 1 and Figure 1). To maximize the observing efficiency, we utilized the HFA array to simultaneously observe the “red” and “blue” positions, while observing for the [C II] line at the “red” and “blue” positions with individual LFA pointings. While both HFA and LFA have seven pixels, given the brightness distribution observed by *Herschel*-PACS (Lee et al. 2014), we expected to detect emission only in the three positions chosen. The observations were performed in Dual Beam Switching mode (DBS). The offset position was 30'' away from L1551 IRS 5, perpendicular to the outflow direction, and observed with a chop frequency of 0.626 Hz. The on-source time for each position and spectral setup is listed in Table 1.

To maximize the bandwidth around the [O I] line, each position was observed with two spectral set ups centered at  $-50 \text{ km s}^{-1}$  and  $+50 \text{ km s}^{-1}$ , denoted as “m50” and “p50”, respectively, to cover  $-100 \text{ km s}^{-1}$  to  $+100 \text{ km s}^{-1}$  around the [O I] line. The “red” position was only observed with the “p50” setup due to the cancellation of a scheduled flight. However, given that only red-shifted emission would be expected at this position anyway, observing only the “p50” setup should have captured most of the emission from the red-shifted outflow. While the HFA was observing the full  $-100 \text{ km s}^{-1}$  to  $+100 \text{ km s}^{-1}$  around the [O I] line with two spectral setups, the LFA only had one spectral setup; as a result, the LFA spectral setups were observed for twice as long as the HFA setup.

We used CLASS (Gildas Team 2013) for data reduction. All spectra were inspected individually, and those associated with backend or receiver instabilities were dropped and not considered for further reduction. SOFIA/upGREAT has a native spectral resolution of 244 kHz, corresponding to 0.015 and 0.039  $\text{km s}^{-1}$  resolution at the [O I] and [C II] lines. We first smoothed the spectrum of each observing block to 1  $\text{km s}^{-1}$ . Then, we fitted the baseline in the line-free region and subtracted it from each spectrum using a first-order polynomial. Finally, we averaged all spectra taken with the same setup together, weighted by their respective noise. The [O I] observations in the “m50” setup were affected by a narrow, but intense, telluric line entering at a velocity of  $-40 \text{ km s}^{-1}$  (in Cycle 7) and  $-14 \text{ km s}^{-1}$  (in Cycle 6). We masked the channels of the atmospheric line in order to remove it from the analysis of the emission.

### 3. RESULTS AND ANALYSES

#### 3.1. [O I] 63 $\mu\text{m}$

To combine two [O I] spectra taken with two setups of local oscillator frequencies (“m50” and “p50”; see Section 2), we took the weighted average of the two spec-

tra using on-source time as the weight. Figure 2 shows the [O I] spectra observed toward the “red,” “center,” and “blue” positions. For the baseline fitting and subtraction, we selected velocity ranges of  $-150 \text{ km s}^{-1} < v_{\text{lsr}} < -110 \text{ km s}^{-1}$  and  $20 \text{ km s}^{-1} < v_{\text{lsr}} < 130 \text{ km s}^{-1}$ . The baseline noise is 0.10 K, 0.15 K, and 0.09 K for the “red,” “center,” and “blue” positions, respectively. The “center” spectrum shows a clear detection of the [O I] 63  $\mu\text{m}$  line, with a peak at around 0–5  $\text{km s}^{-1}$  and a broad blue-shifted tail. We detect no emission at red-shifted velocities at the “center” position. We also do not detect any significant [O I] emission in the “red” or “blue” positions in the outflows. To better characterize the broad blue-shifted feature at the center position, we further smoothed the [O I] spectra to 5  $\text{km s}^{-1}$  resolution. At the “center” position, the smoothed [O I] spectrum shows two tentative local peaks at  $-53 \text{ km s}^{-1}$  and  $-31 \text{ km s}^{-1}$  in addition to the prominent peak around the source velocity. The intensities of these two peaks are roughly equal to the half of the maximum intensity. If these two peaks belong to the same broad feature, the FWHM of the [O I] line is then  $\sim 100 \text{ km s}^{-1}$ . However, if these two peaks are separate features, the primary line profile centered at the source velocity would have a FWHM of  $\sim 40 \text{ km s}^{-1}$  along with two lines at  $-53 \text{ km s}^{-1}$  and  $-31 \text{ km s}^{-1}$  with a width of  $\sim 10 \text{ km s}^{-1}$  each.

#### 3.2. [C II] 158 $\mu\text{m}$

Figure 3 shows the [C II] spectra toward the “red,” “center,” and “blue” positions, where the baseline noise is 0.12 K, 0.09 K, and 0.10 K, respectively. We used the central 80% of the spectral window during baseline fitting to avoid large baseline variation toward the edge of the spectral window. We detect a narrow feature near the source velocity in the “center” and “red” spectra (see Figure 4 for a zoomed-in view). These narrow features have a low signal-to-noise ratio (S/N). By fitting a Gaussian profile, we constrain the narrow feature at  $4.8 \pm 0.3 \text{ km s}^{-1}$  (“center” position) to a width of  $2.3 \pm 0.6 \text{ km s}^{-1}$ , a peak temperature of  $0.39 \pm 0.09 \text{ K}$ , and a S/N of 4.4, while, at the “red” position, the narrow feature is centered at  $6.9 \pm 0.3 \text{ km s}^{-1}$  and is fitted with a width of  $2.8 \pm 0.6 \text{ km s}^{-1}$ , a peak temperature of  $0.40 \pm 0.07 \text{ K}$ , and a S/N of 3.4. We also note that the feature in the “red” spectrum has an asymmetric line profile with the blue side of the line having a steeper profile than the red side.

#### 3.3. Comparison with Previous [O I] 63 $\mu\text{m}$ and [C II] 158 $\mu\text{m}$ Observations

Using *Herschel*/PACS, Green et al. (2016) measured line strengths of  $(4.2 \pm 0.1) \times 10^{-12} \text{ erg s}^{-1} \text{ cm}^{-2}$  for the

**Table 1.** Observed Positions and On-source Times

Name	R.A. (J2000)	Dec. (J2000)	[O I] on-source time (sec.)	[C II] & OH on-source time (sec.)
center	04:31:34.07	18:08:04.90	p50: 132; m50: 165	297
blue	04:31:33.69	18:08:01.10	p50: 554; m50: 229	267
red	04:31:34.46	18:08:08.70	p50: 554; m50: n/a	286

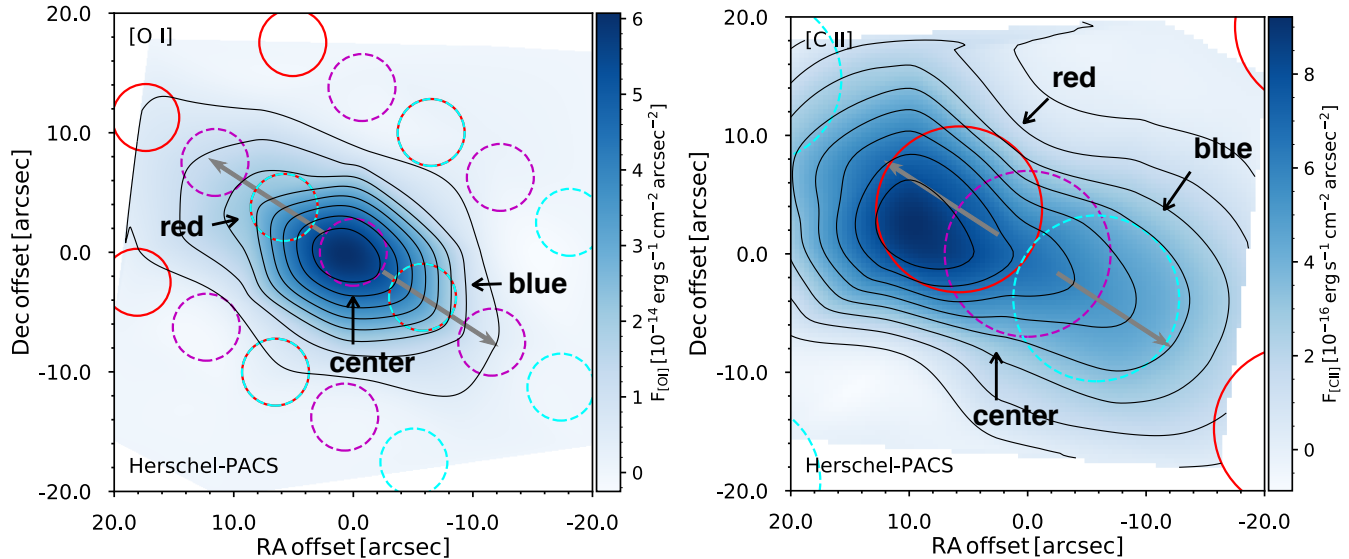


**Figure 1.** The intensity maps of the [O I] 63  $\mu\text{m}$  (left) and [C II] 158  $\mu\text{m}$  (right) lines observed by Herschel-PACS (Lee et al. 2014; Green et al. 2016). The footprints indicate the layouts of HFA and LFA for the [O I] and [C II] lines, respectively. The “red”, “center”, and “blue” positions are annotated. The footprints of the HFA and LFA arrays for the “red”, “center”, and “blue” pointings are shown in red circles, magenta circles, and cyan dashed circles, respectively. The gray arrows denote the outflow direction (position angle =  $57^\circ$ , Wu et al. 2009), red-shifted to the northeast and blue-shifted to the southwest.

[O I] line from a spatial pixel (hereafter spaxel) centered on L1551 IRS 5, which has a size of  $9''.4 \times 9''.4$ . For these SOFIA/upGREAT observations, we derived an integrated line flux at 63  $\mu\text{m}$  of  $(2.2 \pm 0.2) \times 10^{-12}$   $\text{erg s}^{-1} \text{cm}^{-2}$  using a symmetric Gaussian beam ( $\Omega = \theta_{\text{HPBW}}^2 \pi / 4 \ln 2$ ;  $\theta_{\text{HPBW}} = 6''.3$ ). The greater line flux observed with Herschel suggests that the emission extends beyond the SOFIA beam. If we naively assume a uniform brightness distribution and scale the SOFIA line flux to the square PACS spaxel ( $9''.4 \times 9''.4$ ), the line flux becomes  $(4.4 \pm 0.4) \times 10^{-12}$   $\text{erg s}^{-1} \text{cm}^{-2}$ . The consistency indicates that red-shifted emission is also missing in the Herschel observations (see further discussion in Section 4.1).

Using the Kuiper Airborne Observatory (KAO), Cohen et al. (1988) measured an [O I] line flux of  $(5.0 \pm 1.2) \times 10^{-12}$   $\text{erg s}^{-1} \text{cm}^{-2}$  from a  $44''$  aperture, consistent with the measurements using Herschel and SOFIA. Green et al. (2016) measured a total [O I] 63  $\mu\text{m}$  line flux of  $(7.1 \pm 0.1) \times 10^{-12}$   $\text{erg s}^{-1} \text{cm}^{-2}$  over the

entire  $47'' \times 47''$  field of view, consistent with the KAO line flux given the larger aperture.

Green et al. (2016) mapped the [C II] line flux in the  $47'' \times 47''$  region around the protostar using Herschel. From the Herschel intensity map of the [C II] emission (Figure 1, right), we can estimate the [C II] line flux within the SOFIA beam of  $14''.1$ , finding  $1.1 \times 10^{-13}$  and  $1.2 \times 10^{-13}$   $\text{erg s}^{-1} \text{cm}^{-2}$  in the “center” and “red” positions, respectively. The narrow feature in our SOFIA observations have a line flux of  $3.5 \times 10^{-14}$  and  $3.1 \times 10^{-14}$   $\text{erg s}^{-1} \text{cm}^{-2}$  in the “center” and “red” positions, respectively, which only represents 32% and 26% of the total line flux detected with Herschel. This discrepancy hints at a broad [C II] emission undetected in our SOFIA observations or that SOFIA chopped out extended emission more than Herschel did (i.e., observations of SOFIA have more significant [C II] emission at the chopped position than that of Herschel). We further discuss the line width of the undetected [C II] emission in Section 4.3.

#### 4. DISCUSSION



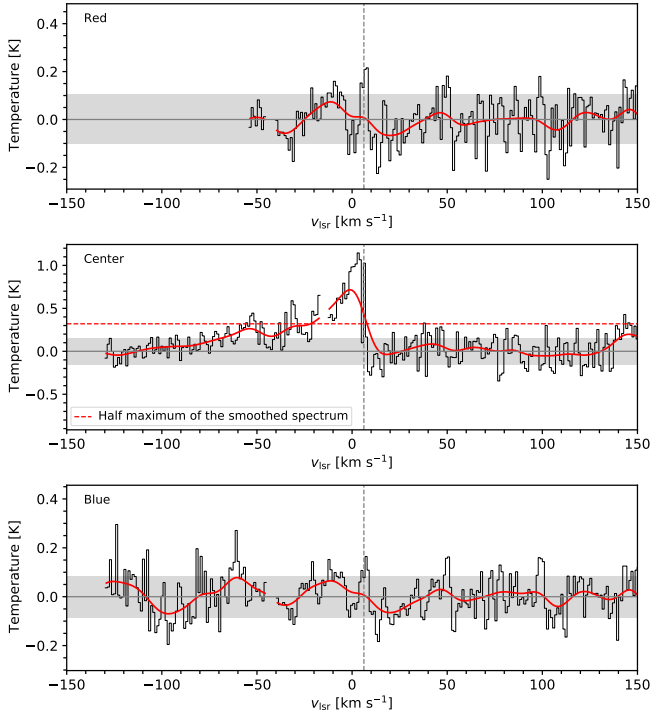


**Figure 2.** The baseline-subtracted [O I] spectra toward the “red,” “center,” and “blue” positions from top to bottom. The black line shows the spectra smoothed to  $1 \text{ km s}^{-1}$ , while the red line shows the spectra smoothed to  $5 \text{ km s}^{-1}$ . The vertical dashed line indicates the source velocity of  $6.2 \text{ km s}^{-1}$ . The horizontal red dashed line in the “center” spectrum illustrates the half maximum of the spectrum smoothed to  $5 \text{ km s}^{-1}$ . The shaded region illustrates the  $\pm 1\sigma$  noise around the baseline. Channels showing telluric features at  $-14$  and  $-40 \text{ km s}^{-1}$  have been masked (see Section 2).

#### 4.1. The Missing Red-shifted [O I] Emission

The [O I] emission at the “central” position shows only blue-shifted emission and no detectable red-shifted emission. However, we expected to detect the emission from both lobes of outflows, resulting in a more symmetric line profile centered at the source velocity. Given this puzzling asymmetric line profile, we consider a few scenarios that may explain our observations. In the case of massive protostars, colder [O I] gas in the surrounding envelope can absorb the emission from warm [O I] originating in the outflow, resulting in absorption features around the envelope velocity, which is similar to the source velocity (Karska et al. 2014b; Leurini et al. 2015). However, in this scenario, the emission should show a rather narrow absorption feature centered at the source velocity, which appears in our observations, and the high-velocity red-shifted [O I] emission should have been detected (like the detected blue-shifted emission). Thus, this scenario is unlikely. Asymmetric outflows where the blue-shifted outflow is much stronger than the

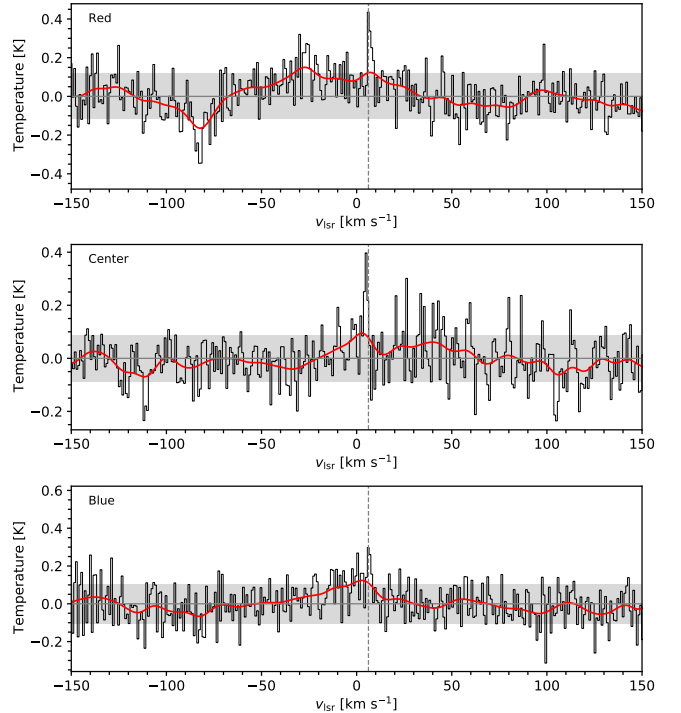


**Figure 3.** Same as Figure 2, but for the baseline-subtracted [C II] spectra toward the “red,” “center,” and “blue” positions from top to bottom.

red-shifted outflow would lead to an asymmetric [O I] line profile, such as the outflow of TMC 1A (Bjerkeli et al. 2016). However, the [O I] emission observed by Herschel appears quite symmetric in both outflow lobes (Figure 1, left), so this scenario is also unlikely.

The circumbinary disk can preferentially block the red-shifted emission if most of the [O I] emission would originate only from the inner  $\sim 300 \text{ au}$  region (Cruz-Sáenz de Miera et al. 2019; Takakuwa et al. 2020). The observed [O I] line profile has a low-velocity ( $\lesssim 20 \text{ km s}^{-1}$ ) and a high-velocity ( $\sim 20\text{--}80 \text{ km s}^{-1}$ ) component (Figure 2; see also Section 4.2). In this scenario, both components would have a scale of  $\lesssim 300 \text{ au}$ . Disk wind may occur at the disk scale ( $r \sim 150 \text{ au}$ ) and could produce the low-velocity component (Ercolano & Owen 2016; Gressel et al. 2020) but not the high-velocity component, which may due to jets. While the jets remain spatially unresolved with our SOFIA observations, the comparison of the [O I] line profile observed by Herschel-PACS and SOFIA finds predominantly blue-shifted emission between the inner  $6''.2$  and  $9''.4$  regions (Figure 5), suggesting that the jet extends beyond the disk scale. The missing red-shifted emission at high-velocity indicates that the obscuration is, in fact, beyond the disk scale; thus, the circumbinary disk is unlikely to be the main obscuration mechanism.

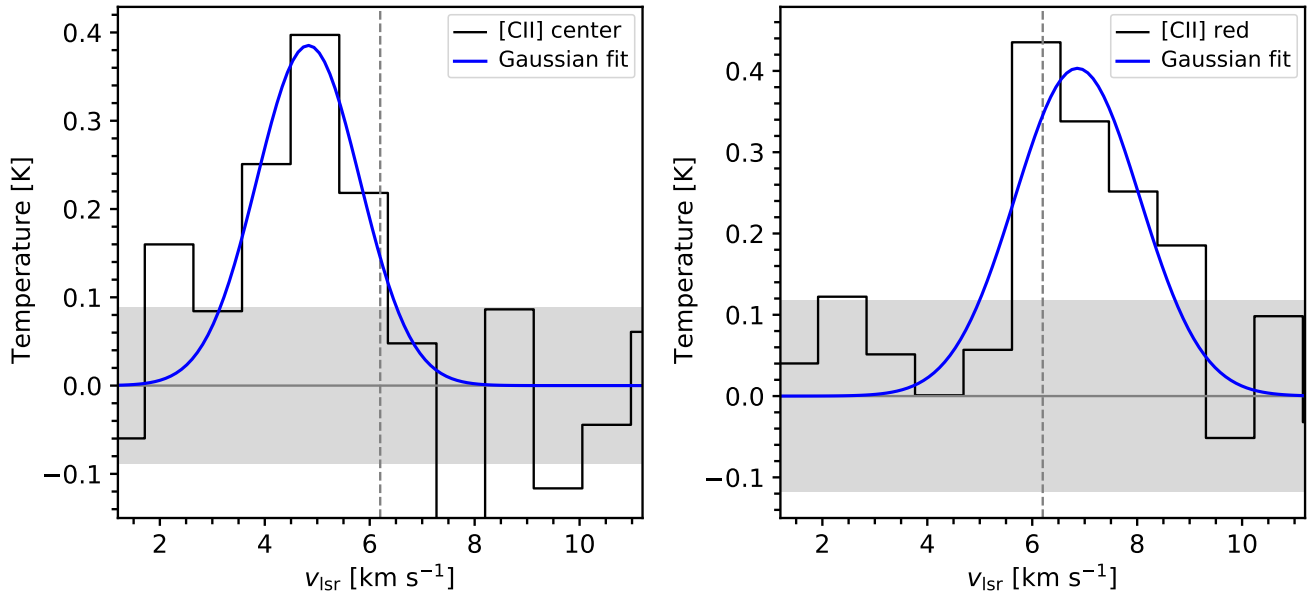


**Figure 4.** The zoomed-in [C II] spectrum at the “center” (left) and “red” positions (right). Only the low velocity emission is shown here. The blue lines indicate the fitted Gaussian profiles. The shaded region illustrates the  $\pm 1\sigma$  noise around the baseline. See Section 3.2 for properties of the fitted lines.

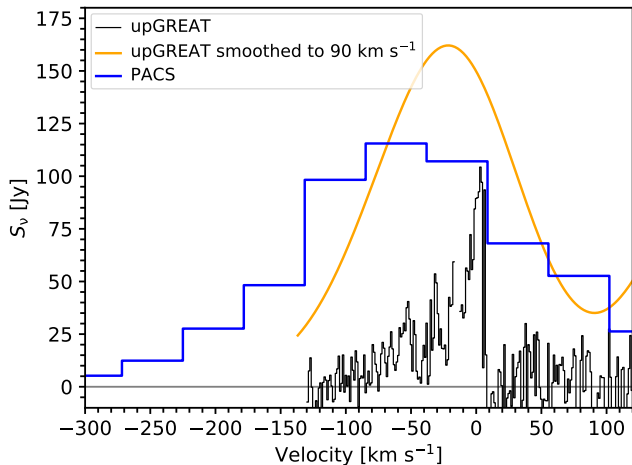


**Figure 5.** The [O I] spectrum at the “center” position compared with the Herschel-PACS [O I] spectrum (blue). The upGREAT spectrum (orange) is smoothed to  $90 \text{ km s}^{-1}$  to match the spectral resolution of PACS. The original upGREAT [O I] spectrum is shown in black for comparison.

Dust in the protostellar envelope can produce differential extinction in the blue- and red-shifted outflows if the outflows are inclined with respect to the plane of the sky. The dust opacity from the envelope would impact the [O I]  $63 \mu\text{m}$  line more than the [O I]  $145 \mu\text{m}$  line because the dust opacity is typically proportional to  $\lambda^{-\beta}$ , where  $\beta$  is often assumed as  $\sim 1.8$ , making the ratio of these two lines an indicator of differential extinction. From the Herschel observations, the ratio of the two [O I] lines increases toward the blue-shifted outflow and de-

creases toward the red-shifted outflow, indicative of significant dust extinction towards the red-shifted outflow (Figure 6). Nisini et al. (2015) performed a similar analysis on other low-mass protostellar outflows but found no obvious variation of the [O I] line ratio. The disappearance of the red-shifted outflow in the 2MASS image of L1551 IRS 5 (Skrutskie et al. 2006) also corroborates the scenario of differential dust extinction (Figure 7).

To quantitatively test the effect of differential extinction, we use the envelope model of L1551 IRS 5 presented in Kristensen et al. (2012), which has a density profile

$$n_{\text{gas}} = n_{\text{in}} \left( \frac{r}{r_{\text{in}}} \right)^{-1.8}, \text{ where } r_{\text{in}} < r < r_{\text{out}}. \quad (1)$$

$r_{\text{in}}$  and  $r_{\text{out}}$  are the inner and outer radius of the envelope, and  $n_{\text{in}}$  is the gas number density at  $r_{\text{in}}$ . By fitting the SED and the radial brightness profiles at  $450 \mu\text{m}$  and  $850 \mu\text{m}$ , Kristensen et al. (2012) constrained these parameters to  $n_{\text{in}} \sim 6.9 \times 10^8 \text{ cm}^{-3}$ ,  $r_{\text{in}} \sim 28.9 \text{ au}$ , and  $r_{\text{out}} \sim 14,000 \text{ au}$ . To model the optical depth toward the blue- and red-shifted outflows, we assume triangular outflow cavities and adopt geometric parameters from the literature.

For example, we adopt an outflow half-opening angle ( $\theta_{\text{cav}}$ ) of  $22^\circ$  (Wu et al. 2009) and an inclination angle ( $\theta_{\text{incl}}$ ) of  $30^\circ$  with respect to the plane of the sky (Chou et al. 2014). Then, to derive the column density ( $N_{\text{gas}}$ ) at any impact parameter ( $b$ ), we can simply integrate the density profile (Equation 1) from either the

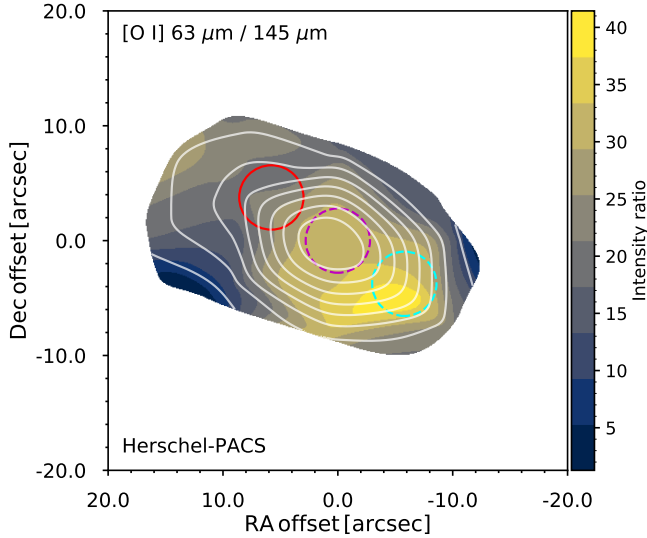


**Figure 6.** Intensity ratio of [O I] 63  $\mu\text{m}$  to 145  $\mu\text{m}$  lines based on interpolating the intensity map from the Herschel observations. The positions where the line flux is less than 20% of the maximum are masked. The white contours show the emission of [O I] 63  $\mu\text{m}$ , while the red solid circle, magenta dashed circle, and cyan dashed circle indicate the “red”, “center”, and “blue” positions.

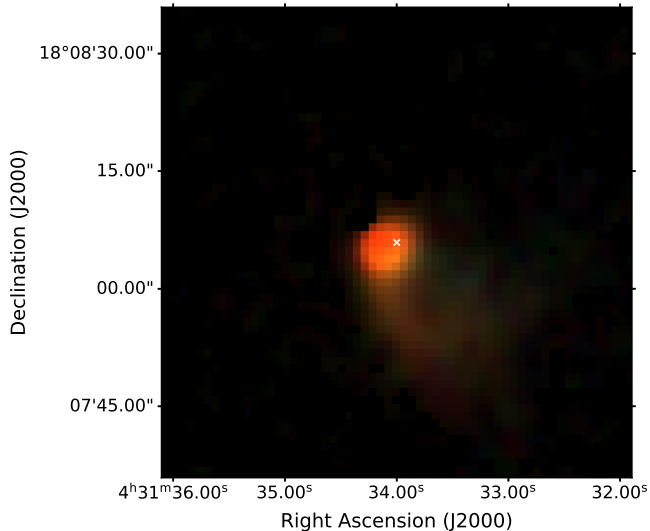


**Figure 7.** An RGB image of L1551 IRS 5 using the 2MASS  $J$ -,  $H$ -, and  $K_s$ -band images as blue, green, and red, respectively. The images are combined using the method described in Lupton et al. (2004) implemented in *ASTROPY*.

inner edge of the envelope,  $\sqrt{r_{\text{in}}^2 - b^2}$ , or the outflow cavity wall,  $b \tan(\theta_{\text{cav}} + \theta_{\text{incl}})$ , to the outer edge of the envelope,  $\sqrt{r_{\text{out}}^2 - b^2}$ . The  $\theta_{\text{cav}}$  is positive for the blue-shifted outflow cavity and negative for the red-shifted outflow cavity. With an estimate of the column density

in hand, we can estimate the dust optical depth from

$$\tau_{\text{dust}} = \kappa_{63 \mu\text{m}} N_{\text{gas}} \mu m_{\text{H}} 0.01, \quad (2)$$

where  $\kappa_{63 \mu\text{m}} = 2.1 \times 10^2 \text{ cm}^{-2} \text{ g}^{-1}$  is the dust opacity at 63  $\mu\text{m}$  taken from Table 1, column 5 in Ossenkopf & Henning (1994),  $\mu = 2.8$  is the mean molecular weight (Kauffmann et al. 2008),  $m_{\text{H}}$  is the mass of a hydrogen atom, and 0.01 is the dust-to-gas mass ratio.

Because the outflow is inclined, the integrated dust optical depth toward the red-shifted outflow is greater than that toward the blue-shifted outflow (Figure 8). Assuming both outflows have the same intrinsic [O I] line flux, the observed flux ratio between two lobes can be approximated by the ratio of  $\Sigma e^{-\tau} \Delta b$ , where  $\tau$  is the dust optical depth in each outflow lobe as presented in Figure 8. The results are given in Figure 9, which shows that the dust extinction from the envelope can significantly reduce the flux ratio to  $\sim 0.55 \pm 0.15$  with a SOFIA beam size of  $6''.3$ . The observed flux ratio upper limit agrees with the modeled ratio within the uncertainty, but is lower than the modeled ratio. If the [O I] emission originates from shocked gas, the [O I] line intensity would be higher toward the protostar, resulting in a lower flux ratio in the model that assumes a uniform brightness. With a resolution of  $9''.4$ , the Herschel/PACS observations (Figure 1) cannot resolve the inner  $\sim 6''$  where the red-shifted outflow is mostly extinguished ( $\tau > 1$  in Figure 8). Beyond the inner  $9''.4$  region, the dust extinction has negligible impact on the [O I] emission, resulting in a rather symmetric distribution of [O I] emission in Figure 1. Thus, extinction due to the dusty envelope surrounding L1551 IRS 5 is the most likely reason for the absence of red-shifted emission in the resolved [O I] line, although the circumbinary disk may block some low-velocity red-shifted [O I] emission. The asymmetric line profiles of CO  $J = 16 \rightarrow 15$  and  $\text{H}_2\text{O } 2_{02} \rightarrow 1_{11}$ , which are discussed in Section 4.2, also corroborate with the extinction due to the envelope. As the wavelength increases, from the CO line to the  $\text{H}_2\text{O}$  line, the asymmetry becomes less obvious (Figure 9).

We further test the extinction from the envelope model using observations of [Fe II] jets in L1551 IRS 5. Hayashi & Pyo (2009) detected a faint [Fe II] jet in the red-shifted outflow, appearing only at separations  $> 10''$  from the protostar. They also measured a visual extinction,  $A_V$ , of 20–30 mag for this faint jet. We estimate the  $A_V$  using the dust opacity at  $0.55 \mu\text{m}$  ( $2.1 \times 10^4 \text{ cm}^2 \text{ g}^{-1}$ ) and taking  $A_V = 2.5 \log_{10}(e^{\tau_V}) = 1.086 \tau_V$ . Figure 10 shows the  $A_V$  along the red- and blue-shifted outflows. At an offset  $> 10''$ , the  $A_V$  toward the red-shifted outflows is consistent with the  $A_V$  measured from

the [Fe II] jet, supporting the scenario of envelope extinction for the [O I] line.

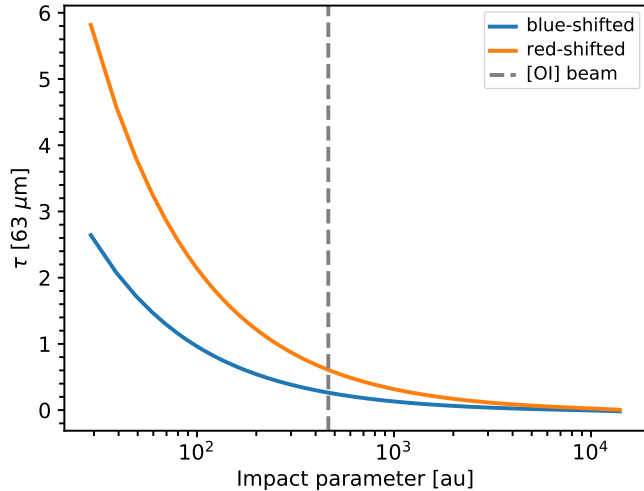


**Figure 8.** Dust optical depth as a function of impact parameters in the blue- and red-shifted outflows. The gray dashed line indicates the beam radius of the SOFIA observations,  $3''.15$ , at a distance of 147.3 pc.

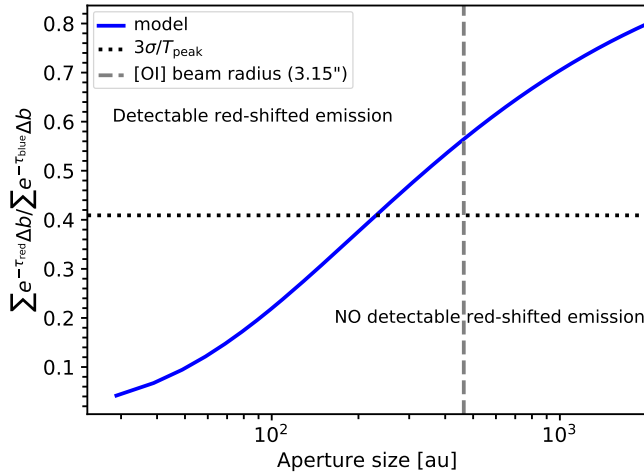


**Figure 9.** Ratio of the integrated optical depth correction factors in the red- and blue-shifted outflows as a function of aperture size. The gray dashed line indicates the beam radius at  $63 \mu\text{m}$ . The dotted line indicates the ratio of the  $3\sigma$  limit on the [O I] emission to the peak intensity of the emission at the “center” position, while the shaded region indicates the uncertainty of the ratio.

#### 4.2. Shocks as the Origin of the [O I], CO, and H<sub>2</sub>O Emission

The broad line width and significant velocity offset of the [O I] line profile suggests an outflow origin. From

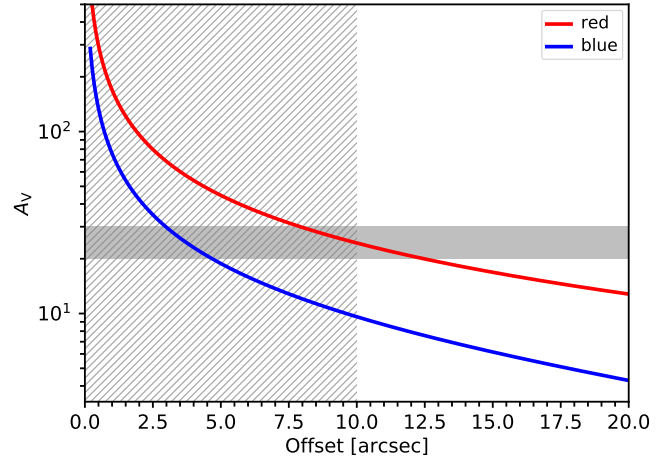


**Figure 10.** Visual extinction ( $A_V$ ) as a function of radius for the envelope model. The red and blue lines show the  $A_V$  along the red- and blue-shifted outflows, respectively. The hatched region highlights the area where Hayashi & Pyo (2009) found no signature of jets toward the red-shifted outflow and the gray area indicates their estimated  $A_V$  from the faint jet detected at  $>10''$  from the protostar.

observations of far-infrared emission in outflows, a composite scenario emerges from high- $J$  CO and H<sub>2</sub>O lines (e.g., Kristensen et al. 2012, 2017b; Mottram et al. 2017; Karska et al. 2018; Yang et al. 2018). In this scenario, the outflow-envelope interaction leads to shock-excited emission of high- $J$  CO, H<sub>2</sub>O, and [O I] lines. So-called “cavity” shocks at the envelope-outflow interface can produce broad (typical FWHM of  $> 15 \text{ km s}^{-1}$ ) emission centered at the source velocity, while “spot” shocks occurring within the outflow (typical FWHM of  $= 5 - 15 \text{ km s}^{-1}$ ) result in emission that is offset from the source velocity, and often blue-shifted. Magneto-hydrodynamical disk winds can also produce similar features as the cavity shocks (Yvart et al. 2016). Some sources show a component similar to that of spot shocks but with significant velocity offset, and are often called Extremely High Velocity (EHV) gas or “bullets”. Both components are thought to originate from spot shocks, likely tracing dissociative J-shocks (Mottram et al. 2014; van Dishoeck et al. 2021). Colder molecular gas entrained by outflows along the edges of the cavity mostly dominates the emission of low- $J$  CO lines, such as CO  $J = 3 \rightarrow 2$ , showing a narrow (FWHM  $< 5 \text{ km s}^{-1}$ ) line profile centered on the source velocity (Yıldız et al. 2013, Figure 11).

The [O I]  $63 \mu\text{m}$  line profile in the “center” position seems to have two components as well, including a component centered at the source velocity with its red-shifted part blocked by the dusty envelope (see discussion in Section 4.1) and a broad component at high blue-



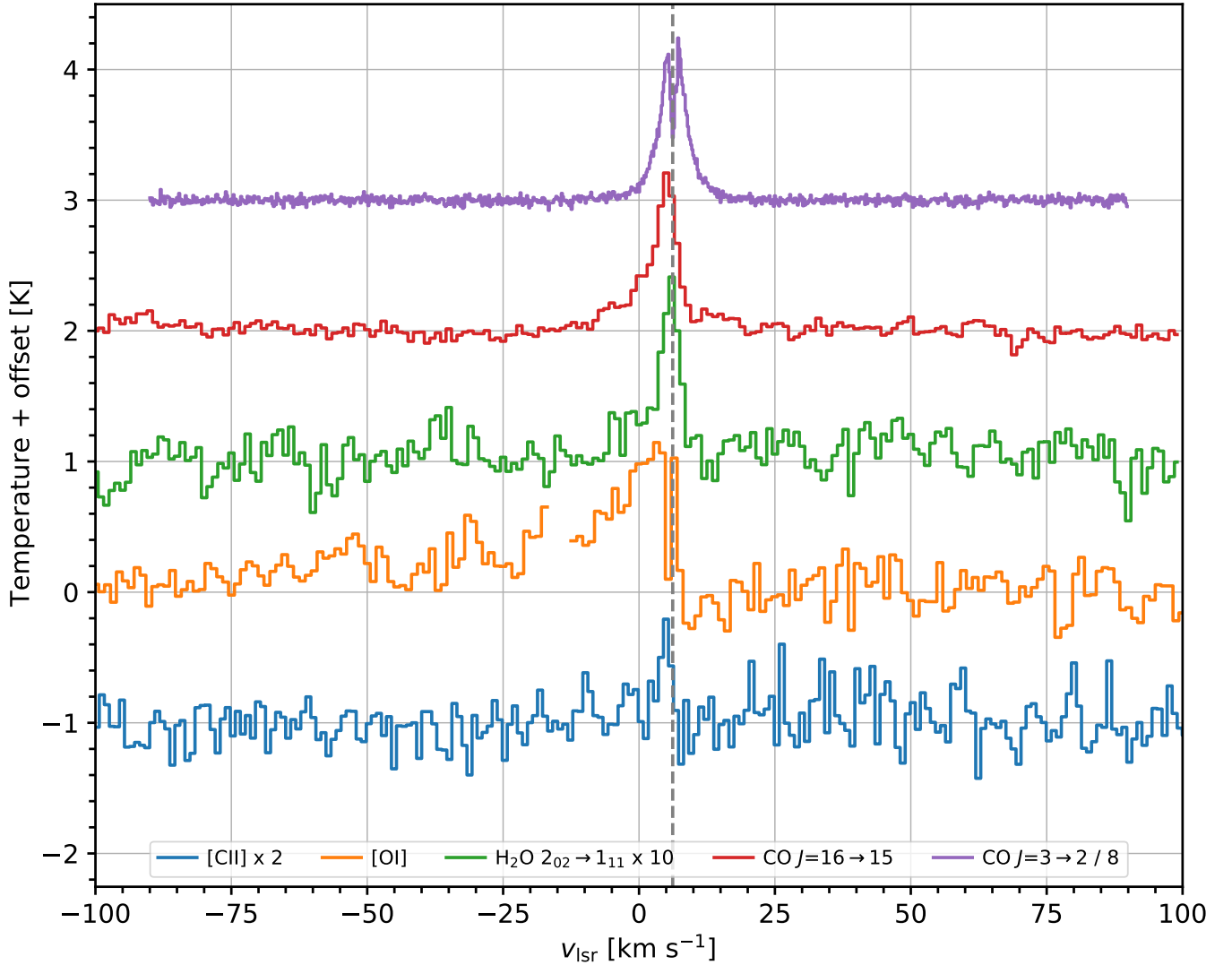


**Figure 11.** Spectra of CO  $J = 3 \rightarrow 2$ , CO  $J = 16 \rightarrow 15$ , H<sub>2</sub>O  $2_{02} \rightarrow 1_{11}$ , [O I]  $63 \mu\text{m}$ , and [C II]  $158 \mu\text{m}$  lines toward the “center” position (from top to bottom). Each spectrum is offset by 1 K for better visualization. The dashed line indicates the source velocity of  $6.2 \text{ km s}^{-1}$ .

shifted velocity. Assuming a two-component model, we fitted two Gaussian profiles with one component fixed at the source velocity,  $6.2 \text{ km s}^{-1}$ , and constrained another broad component at  $-30.0 \text{ km s}^{-1}$  (Figure 12). Table 2 lists the fitted parameters of the two Gaussian profiles. This composite model successfully reproduces the observed line profile, suggesting two distinct components of [O I] gas; however, the fitted parameters of the extremely broad component have  $\sim 35\text{--}60\%$  uncertainties.

Kristensen et al. (2017b) decomposed the Herschel/HIFI CO  $J = 16 \rightarrow 15$  emission in L1551 IRS 5 into two components tracing different physical components. The component that is centered around the source velocity has a narrow line width of  $3.6 \text{ km s}^{-1}$ , and traces the entrained gas. Another component at  $3.6 \text{ km s}^{-1}$  has a width of  $14.9 \text{ km s}^{-1}$  and traces the cavity

shocks (Figure 12). In comparison, the [O I] emission has no narrow component in emission but does show a narrow absorption near the source velocity (at  $\sim 5.4 \text{ km s}^{-1}$ ). This narrow absorption may come from the colder [O I] gas in the quiescent or the infalling envelope. The broad component in CO  $J = 16 \rightarrow 15$  has a similar line profile to the [O I] component centered at the source velocity. The centroid of the CO broad component is  $3.5 \text{ km s}^{-1}$ , which is consistent with the [O I] component centered at the source velocity given the uncertainty in the [O I] spectrum, suggesting that both lines trace the component.

Four H<sub>2</sub>O lines were detected by Herschel (Kristensen et al. 2012; Mottram et al. 2014). The  $2_{02} \rightarrow 1_{11}$  and  $2_{11} \rightarrow 2_{02}$  lines show a narrow component (FWHM =  $4.3 \pm 0.8 \text{ km s}^{-1}$ ) centered at the source velocity

with a blue-shifted line wing (the  $\text{H}_2\text{O } 2_{02} \rightarrow 1_{11}$  emission is shown in Figure 11). However, the other two  $\text{H}_2\text{O}$  lines,  $1_{11} \rightarrow 0_{00}$  and  $1_{10} \rightarrow 1_{01}$ , show a broad ( $\text{FWHM} = 26.1 \pm 6.3 \text{ km s}^{-1}$ ) red-shifted component at  $19.2 \pm 3.0 \text{ km s}^{-1}$  but no narrow component. Figure 12 also shows the decoupled components derived from  $\text{H}_2\text{O}$  lines (Mottram et al. 2014) and the blue-shifted component from a double-Gaussian fit to the  $\text{H}_2\text{O } 2_{02} \rightarrow 1_{11}$  line (Figure 12). At blue-shifted velocities, the  $\text{H}_2\text{O}$  lines in L1551 IRS 5 support a similar scenario as the  $\text{CO } J = 16 \rightarrow 15$  line, where the emission comes from entrained gas and cavity shocks traced by the blue-shifted line wing. At red-shifted velocities, the  $\text{H}_2\text{O}$  lines show a velocity component at  $19.2 \pm 3.0 \text{ km s}^{-1}$  with a width of  $26.1 \pm 6.3 \text{ km s}^{-1}$ , suggesting an origin in cavity shocks (Mottram et al. 2014). The reason why the four  $\text{H}_2\text{O}$  lines exhibit different kinematics remains unclear. A slightly blue-shifted narrow absorption also appears in the  $1_{11} \rightarrow 0_{00}$   $\text{H}_2\text{O}$  line, indicative of absorption by a colder envelope (Mottram et al. 2014).

Among the spectra of high- $J$   $\text{CO}$ ,  $\text{H}_2\text{O}$ , and  $[\text{O I}]$ , only the  $[\text{O I}]$  emission has the extremely broad component with a width of  $\sim 90 \text{ km s}^{-1}$ . Combining the insights learned from the  $[\text{O I}] 63 \mu\text{m}$  and  $\text{CO } J = 16 \rightarrow 15$  lines, a revised picture of the L1551 IRS 5 outflow emerges: The narrow ( $\text{FWHM} = 3.6 \text{ km s}^{-1}$ ) component traces entrained material that appears in emission for  $\text{CO } J = 16 \rightarrow 15$  and  $\text{H}_2\text{O}$  (Mottram et al. 2014). The quiescent envelope appears as narrow absorption seen in both the  $\text{H}_2\text{O } 1_{11} \rightarrow 0_{00}$  line and the  $[\text{O I}] 63 \mu\text{m}$  line. The broad component ( $\text{FWHM} \sim 20 \text{ km s}^{-1}$ ) comes from the cavity shocks where the outflow drives shocks into the cavity walls. The extremely broad component ( $\text{FWHM} \sim 90 \text{ km s}^{-1}$ ) that is only seen in  $[\text{O I}]$  traces J-type spot shocks in the outflow cavity or the jet. The line profiles of all three species,  $[\text{O I}]$ , high- $J$   $\text{CO}$ , and  $\text{H}_2\text{O}$ , show asymmetries that agree with the extinction due to the envelope (see Section 4.1).

Green et al. (2016) detected  $[\text{O I}]$  emission at 63 and 145  $\mu\text{m}$  using Herschel/PACS, further constraining the excitation condition of  $[\text{O I}]$  in L1551 IRS 5. The ratio of  $[\text{O I}] 63 \mu\text{m}/145 \mu\text{m}$  is  $32.0 \pm 4.4$  for the central spaxel and  $25.4 \pm 2.5$  for the 1D spectrum extracted with a  $24''/8$  aperture, which best matches the SPIRE spectrum (Yang et al. 2018, see also Figure 6 for the map of ratios). Nisini et al. (2015) modeled the ratio of the  $[\text{O I}] 63 \mu\text{m}$  to 145  $\mu\text{m}$  lines, which increases with the density of collision partners, suggesting a  $\text{H}_2$  density of  $\sim 10^{5.5} \text{ cm}^{-3}$  for the  $[\text{O I}]$  outflow.

The study of the R1 position in the outflow of NGC 1333 IRAS 4A is a notable comparison to L1551 IRS 5 (Kristensen et al. 2017a). In R1, the  $[\text{O I}] 63 \mu\text{m}$  emis-

**Table 2.** The fitted Gaussian components in the “central”  $[\text{O I}]$  emission

Velocity centroid ( $\text{km s}^{-1}$ )	Integrated flux ( $\text{K km s}^{-1}$ )	Width ( $\text{km s}^{-1}$ )
$6.2^a$	$18.9 \pm 6.3$	$21.0 \pm 4.9$
$-30.0 \pm 19.6$	$25.4 \pm 11.3$	$87.5 \pm 32.3$

<sup>a</sup>The centroid is fixed to the source velocity.

sion observed by SOFIA has a similar line profile as that of  $\text{H}_2\text{O}$  and high- $J$   $\text{CO}$  lines, which are tracers of shocks, suggesting that this emission lines mostly come from the outflows. In contrast, the  $\text{H}_2\text{O}$  line in L1551 IRS 5 has a different line profile compared to the  $[\text{O I}]$  spectrum, suggesting that the  $[\text{O I}]$  emission uniquely trace an atomic outflow and/or jet.

#### 4.3. The Spatial Extent of Shocks and its Connection to UV Radiation

Both shocked gas in outflows and photodissociation regions (PDRs) can contribute to the  $[\text{O I}]$  emission (Hollenbach 1985; Tielens & Hollenbach 1985). Although our SOFIA observations did not detect significant  $[\text{O I}]$  emission at “red” and “blue” outflow positions, Green et al. (2016) detected extended  $[\text{O I}]$  emission with Herschel/PACS on  $\sim 20''$  scales (Figure 1). Interpolating from the Herschel  $[\text{O I}]$  emission map, we estimate  $[\text{O I}]$  velocity-unresolved fluxes of  $7.7 \times 10^{-13}$  and  $7.6 \times 10^{-13} \text{ erg s}^{-1} \text{ cm}^{-2}$  in the “red” and “blue” positions, respectively. If the  $[\text{O I}]$  flux observed by Herschel comes from a single line, our SOFIA observations have a better sensitivity to detect a narrow ( $\text{FWHM} \lesssim 5 \text{ km s}^{-1}$ ) line from PDRs compared to a broad line due to shocks. The non-detection of narrow  $[\text{O I}]$  emission in all three pointings allows us to constrain the maximum contribution to the  $[\text{O I}]$  emission from PDRs by comparing the non-detection to the interpolated  $[\text{O I}]$  flux from Herschel/PACS.  $[\text{C II}]$  emission is a common tracer of PDRs (Hollenbach & Tielens 1999; Kaufman et al. 1999). If we take the mean  $\text{FWHM}$  of the narrow  $[\text{C II}]$  lines,  $2.5 \text{ km s}^{-1}$ , as the characteristic line width of gas in PDRs, the upper limit of the  $[\text{O I}]$  line flux is then  $2.4 \times 10^{-14} \text{ erg s}^{-1} \text{ cm}^{-2}$  at both outflow positions and  $3.7 \times 10^{-14} \text{ erg s}^{-1} \text{ cm}^{-2}$  at the central position. Comparing to the Herschel  $[\text{O I}]$  line fluxes estimated within the “central” (from Section 3.3), “red”, and “blue” positions, the upper limit of the PDR contribution to the  $[\text{O I}]$  flux is 3.1% in “red” and “blue” positions, while the contribution to the  $[\text{O I}]$  flux is 2.6% in the “central” position, suggesting that the shocked gas (i.e., broad emission) dominates the  $[\text{O I}]$  flux. Assuming that a single Gaussian line profile can describe all

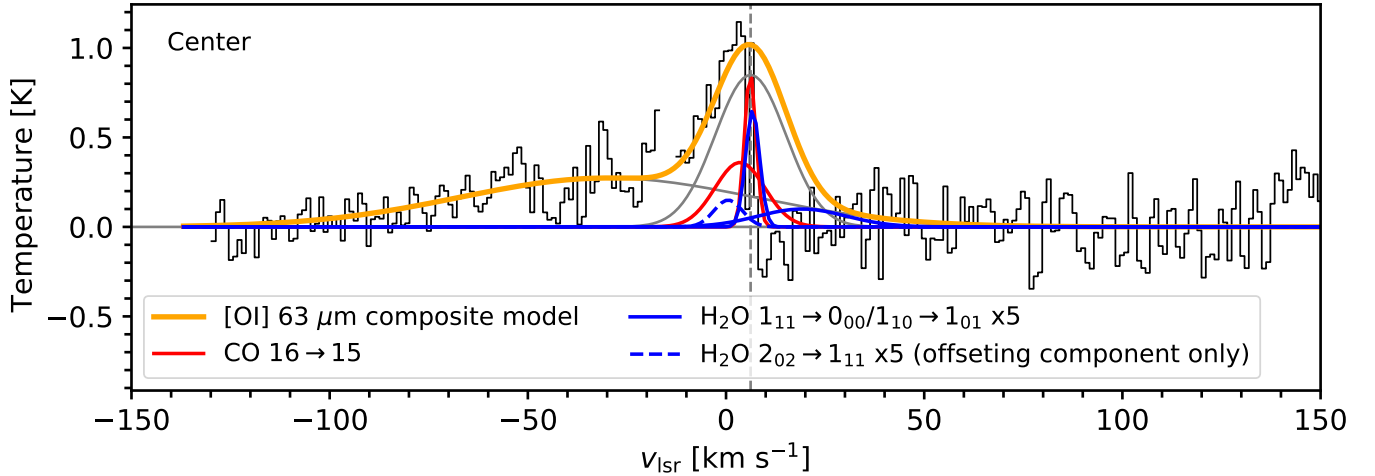


**Figure 12.** The “central” [O I] spectrum (black) along with the best-fitting double Gaussian model. The gray lines indicate each Gaussian component, while the orange line shows the composite model. The FWHMs of the two components are  $21.0 \pm 4.9$   $\text{km s}^{-1}$  and  $87.5 \pm 32.3$   $\text{km s}^{-1}$ , respectively. The red lines show the decoupled components of the CO  $J = 16 \rightarrow 15$  line from Kristensen et al. (2017b) with a narrow component with a width of  $3.6$   $\text{km s}^{-1}$  at  $6.1$   $\text{km s}^{-1}$  and a relatively broad component with a width of  $14.9$   $\text{km s}^{-1}$  at  $3.4$   $\text{km s}^{-1}$ . The blue lines show the decoupled components of the multiple H<sub>2</sub>O lines. Mottram et al. (2014) derived a narrow component at  $6.7$   $\text{km s}^{-1}$  with a FWHM of  $4.2$   $\text{km s}^{-1}$  and a red-shifted broad component at  $19.2$   $\text{km s}^{-1}$  with a FWHM of  $26.1$   $\text{km s}^{-1}$  from the H<sub>2</sub>O  $1_{11} \rightarrow 0_{00}$  and  $1_{10} \rightarrow 1_{01}$  lines (solid blue lines). The blue-shifted component centers on  $0.54$   $\text{km s}^{-1}$  with a FWHM of  $8.4$   $\text{km s}^{-1}$ , fitted from the H<sub>2</sub>O  $2_{02} \rightarrow 1_{11}$  line using CLASS (blue dashed line). The intensity of the H<sub>2</sub>O components are multiplied by five for a better visualization. The vertical dashed line indicates the source velocity at  $6.2$   $\text{km s}^{-1}$ .

the non-PDR [O I] emission, [O I] emission at “red” and “blue” positions should have FWHM greater than  $\sim 80$   $\text{km s}^{-1}$  had it been detected, which is similar to the line width of the extremely broad [O I] component at the “central” position.

The narrow line width of the observed [C II] emission indicates a PDR origin. Extracting the line flux from the Herschel intensity map (Figure 1, right) using the SOFIA beam ( $14''.1$  at the [C II] line), the detected narrow feature makes up 30% and 26% of the total Herschel [C II] flux at the “center” and “red” positions, respectively. If the [C II] emission from the large-scale cloud is removed by beam-chopping (see Section 2), the detected [C II] line flux then traces the emission from local PDRs. The PDRs contribute  $\sim 30\%$  of the total [C II] flux but only represents  $\lesssim 3\%$  of the [O I] flux, suggesting that [O I] emission is indeed a good tracer of shocked gas and the contribution from PDRs is negligible. Furthermore, the spatial extent of the [O I] emission coincides with the blue-shifted [Fe II] emission that unambiguously traces dissociative shocks in the jets (Pyo et al. 2009). If the discrepant [C II] emission between observations of SOFIA and Herschel is instead due to excessive baseline subtraction during data reduction, we can assume a Gaussian profile for the undetected [C II] emission and estimate the lower limit of its line width given the spectral noise. We estimate that the [C II]

flux missing in the SOFIA observations is  $7.7 \times 10^{-14}$  and  $8.9 \times 10^{-14}$   $\text{erg s}^{-1} \text{cm}^{-2}$ , resulting in a lower limit of  $23.3$  and  $20.2$   $\text{km s}^{-1}$  for the line width at the “center” and “red” positions, respectively. Comparing to the lower limit of the [O I] line width, the undetected [C II] emission could be narrower than the undetected [O I] emission.

With the PDR contribution constrained toward the protostar, we can further use the line ratio between [C II] and [O I] to infer the UV radiation incident on the PDR. Karska et al. (2018) calculated the ratio between the [C II]  $158 \mu\text{m}$  and the [O I]  $63 \mu\text{m}$  lines as a function of  $G_0$  from  $10^1$ – $10^{6.5}$  and densities from  $10^3$ – $10^7$   $\text{cm}^{-3}$ . For the PDR contribution in the “center” position, we measure a [C II] line flux of  $3.3 \times 10^{-14}$   $\text{erg s}^{-1} \text{cm}^{-2}$  in a  $14''.1$  beam, and an upper limit of the [O I] line flux of  $3.7 \times 10^{-14}$   $\text{erg s}^{-1} \text{cm}^{-2}$  in a  $6''.3$  beam. Thus, if we scale the [O I] upper limit to the [C II] beam size, we have a lower limit of 0.17 on the ratio of [C II] and [O I]. The corresponding [C II] integrated line intensity is  $9.0 \times 10^{-6}$   $\text{erg s}^{-1} \text{cm}^{-2} \text{sr}^{-1}$  and, combining with the [C II] intensity, we estimate that the incident UV radiation,  $G_0$ , is at most  $\sim 10$  for a density of  $\sim 10^5$   $\text{cm}^{-3}$ , which is similar to the density estimated from the ratio of [O I]  $63 \mu\text{m}$  and  $145 \mu\text{m}$  lines (see Section 4.2; Nisini et al. 2015).

A strength of  $\sim 10$  for the UV radiation is consistent with prior estimates for low-mass protostars, which assumed that 90% of unresolved [O I] emission originates from shocks and 10% from PDRs (Karska et al. 2018). The velocity-resolved line profiles from SOFIA-upGREAT verify such assumptions by identifying the narrow and broad components in [O I] and [C II] lines.

#### 4.4. Chemical Abundance

Besides being a good tracer of energetic outflows and jets, atomic oxygen is a major carrier of volatile oxygen in protostellar shocks. The Herschel Key Program, Water In Star-forming regions with Herschel (WISH), demonstrated that CO, H<sub>2</sub>O, and atomic O represent most of the volatile oxygen budget in protostellar outflows and shocks, but up to 50% of the total oxygen abundance remains unaccounted for (van Dishoeck et al. 2021, and references therein). Velocity-resolved spectra of [O I], CO  $J = 16 \rightarrow 15$ , and H<sub>2</sub>O give us a unique opportunity to identify the emission from shocks as well as to quantify the column density of each oxygen carrier in shocks. The two components of the [O I] emission (Table 2) represent two types of shocks. The broad component (FWHM  $\sim 15 - 25$  km s<sup>-1</sup>) seen in [O I], CO  $J = 16 \rightarrow 15$ , and H<sub>2</sub>O trace cavity shocks, while the extremely broad component only seen in [O I] probes the shocked gas in jets. The absence of an extremely broad component in the high- $J$  CO and H<sub>2</sub>O lines indicates fully dissociative shocks. Tracing the ionized jet, the [Fe II] emission from the ionized jet exhibits an extremely broad (FWHM = 150–180 km s<sup>-1</sup>) component centered at  $\sim -120$  km s<sup>-1</sup> and a narrower (FWHM = 40 km s<sup>-1</sup>) component at  $-300$  to  $-400$  km s<sup>-1</sup> (Pyo et al. 2009). While our observations only show the far-infrared [O I] line up to  $\sim -100$  km s<sup>-1</sup>, the optical [O I] line at 6364 Å has a broad (FWHM  $\sim 200$  km s<sup>-1</sup>) line at  $\sim -100$  to  $-300$  km s<sup>-1</sup> similar to that characteristics of the [Fe II] emission (White & Hillenbrand 2004), suggesting that both [O I] and [Fe II] trace the jet. The brightness of this extremely high-velocity component likely falls below the sensitivity of our observations.

We can further estimate the oxygen budget in the shocks. To estimate the [O I] column density for the broad component centered at the source velocity (Figure 13, orange line), we used the non-LTE radiative transfer code, RADEX (van der Tak et al. 2007) and the collision rates from Leiden Atomic and Molecular Database (LAMDA Schöier et al. 2005). While the ratio of [O I] 63  $\mu$ m and 145  $\mu$ m line fluxes indicates a H<sub>2</sub> density of  $10^{5.5}$  cm<sup>-3</sup> (Nisini et al. 2015), both the kinetic temperature ( $T_{\text{kin}}$ ) and the column density of

[O I] remains unknown. Using the line fitting results listed in Table 2, we modeled an [O I] column density of  $(1-5) \times 10^{16}$  cm<sup>-2</sup> with a kinetic temperature ranging from 500 to 8000 K (Figure 13). The modeling used the [O I] atomic data from the Leiden Atomic and Molecular Database (Schöier et al. 2005) and assumed a uniform geometry for calculating the escape probability to reproduce the observed [O I] line flux within 1%. The collision rates from LAMDA only cover the first three states of [O I]. To test the necessity of including higher states that produce the 6300 Å and 6364 Å lines, we further include the <sup>1</sup>D<sub>2</sub> and <sup>1</sup>S<sub>0</sub> states using Table F.3 and Equation 2.27 of Draine (2010), which employs the data from Pequignot (1990). Assuming a typical electron density of  $2 \times 10^4$  cm<sup>-3</sup> in protostellar jets (Hartigan et al. 2019), the calculations with the updated collision rates show that these excited states have negligible impact on the atomic oxygen column density derived from the <sup>3</sup>P<sub>1</sub>  $\rightarrow$  <sup>3</sup>P<sub>2</sub> transition. The uncertainty of the [O I] column density is  $\sim 40\%$  due to the uncertainty in the measured flux. The modeled [O I] column density only varies by a factor of  $\sim 2$  in  $8000 \text{ K} > T_{\text{kin}} > 750 \text{ K}$ . Because both atomic and molecular lines are present in the cavity shocks, the temperature has to be moderate to prevent dissociation. Therefore, we assume that the cavity shocks in L1551 IRS 5 have the same temperature as the shocks in NGC 1333 IRAS 4A R1, 750 K (Kristensen et al. 2017a), which then gives a [O I] column density of  $(2.0 \pm 0.7) \times 10^{16}$  cm<sup>-2</sup>. Assuming a temperature of 750 K and a H<sub>2</sub> density of  $10^{5.5}$  cm<sup>-3</sup>, we can also model the broad component of the CO and H<sub>2</sub>O emission using RADEX. For the CO  $J = 16 \rightarrow 15$  line, the broad (FWHM = 14.9 km s<sup>-1</sup>) component has a peak intensity of 0.36 K (Figure 12), resulting in a column density of  $(2.7 \pm 0.2) \times 10^{15}$  cm<sup>-2</sup>. For H<sub>2</sub>O, we modeled the red- and blue-shifted components separately. The modeling suggests a column density of  $(5.1 \pm 2.6) \times 10^{12}$  cm<sup>-2</sup> for the red-shifted component in the 1<sub>11</sub>  $\rightarrow$  0<sub>00</sub> line with a FWHM of 26.1 km s<sup>-1</sup> and a peak intensity of 0.02 K; the modeling meanwhile gives a column density of  $(5.0 \pm 2.3) \times 10^{12}$  cm<sup>-2</sup> for the blue-shifted component in the 2<sub>02</sub>  $\rightarrow$  1<sub>11</sub> line with a FWHM of 8.4 km s<sup>-1</sup> and a peak intensity of 0.03 K.

To derive the abundance of dominant oxygen carriers, we need to estimate the mass of each species in the same location. Because of the different beam sizes for [O I], CO, and H<sub>2</sub>O observations, we examine two scenarios to derive the range of possible abundances. First, we assume that the shocks are spatially unresolved for all three lines. In this case, we can derive the mass of each species by multiplying the column density with the respective beam size. The SOFIA beam for [O I] is 6''3 and

the Herschel beams for CO  $J = 16 \rightarrow 15$  and H<sub>2</sub>O lines are 11''5 and 22'', respectively. The relative abundance of each species can be written as

$$\frac{X(Y)}{X(O_{\text{total}})} = \frac{N(Y)\Omega_Y}{N(O)\Omega_O + N(\text{CO})\Omega_{\text{CO}} + N(\text{H}_2\text{O})\Omega_{\text{H}_2\text{O}}}, \quad (3)$$

where  $\Omega_Y$  is the beam area for the observations of each species. In the second scenario, we assume the shocks are uniformly spread out over the beam. A larger beam would probe more shocked gas. Therefore, we derive the abundance of each species using the smallest beam size (i.e., 6''3 for [O I]) instead of their respective beams. In both cases, we assume that all three species trace the same shocks. Furthermore, we only consider the gaseous oxygen carriers and the refractory oxygen remains locked on dust grains because of the SiO non-detection (Codella et al. 1999). Any refractory oxygen released from dust grains will make the relative abundances in Table 3 upper limits.

For cavity shocks and/or disk winds, atomic oxygen is the primary carrier of oxygen, representing 69% and 88% of the gaseous oxygen abundance in the extended and unresolved scenarios, respectively, with CO as the secondary oxygen carrier (Table 3).

To estimate the absolute abundances of these major oxygen carriers, we need to make assumptions about the total gaseous oxygen abundance. There is a long-standing problem of missing oxygen, where the elemental oxygen abundance in the interstellar medium,  $5.8 \times 10^{-4}$  (Przybilla et al. 2008), is consistently higher than all the observable oxygen carriers in star-forming regions (e.g., van Dishoeck et al. 2021). This so-called undetected depleted oxygen (UDO) abundance with respect to H is  $\sim 1\text{--}2 \times 10^{-4}$  in star-forming regions (van Dishoeck et al. 2021). If we assume a UDO abundance of  $2 \times 10^{-4}$ , the remaining volatile oxygen abundance is  $3.8 \times 10^{-4}$ , similar to the value of  $(3.4 \pm 0.5) \times 10^{-4}$  measured from using translucent sight lines toward stars (Sofia et al. 2004). Furthermore, refractory dust also carries oxygen. Following the assumption made in van Dishoeck et al. (2021), we assume a refractory abundance of  $1.4 \times 10^{-4}$  derived from the Mg, Si, and Fe abundances in Przybilla et al. (2008). Henceforth, we assume a total gaseous oxygen abundance of  $2.0 \times 10^{-4}$ . From Equation 3, we then derive an atomic oxygen abundance relative to H for the two scenarios described above (“extended” and “unresolved” in Table 3). The dominant presence of [O I] is expected in L1551 IRS 5; Karska et al. (2018) found the [O I] luminosity dominates the line luminosity of major coolants, such as H<sub>2</sub>O, CO, and OH. In L1551 IRS 5, the [O I] luminosity takes up 55% of the total line luminosity, while the warm and hot

CO luminosity takes up 38%. The  $X(\text{O})$  is shockingly high compared to the oxygen abundance in other observations of protostellar shocks. In the R1 shock knot of NGC 1333 IRAS 4A, for instance, Kristensen et al. (2017a) analyzed the velocity-resolved [O I] emission and estimated an  $X(\text{O})$  of  $5\text{--}6 \times 10^{-5}$ , taking up only  $\sim 15\%$  of the total oxygen volatile abundance.

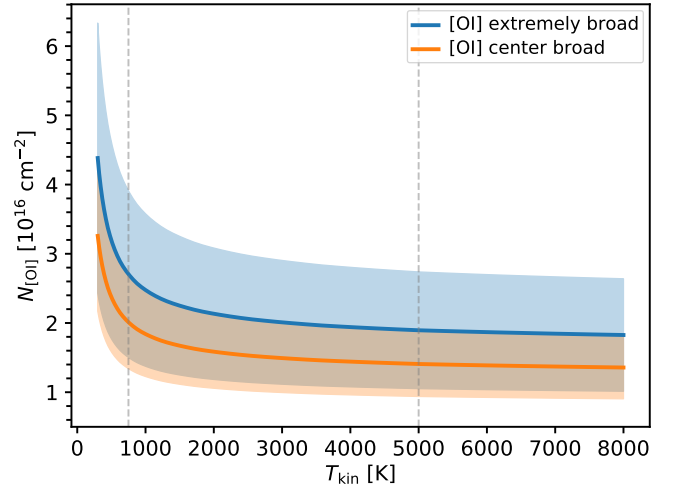


**Figure 13.** The best-fitting [O I] column density from the RADEX non-LTE modeling. The orange and blue lines show the fitting results for the broad component at the source velocity and the extremely broad component, respectively. The shaded region represents the uncertainty due to the noise in the spectra. The vertical dashed lines highlight  $T_{\text{kin}} = 750$  K and 5000 K, relevant for cavity and J-shocks in the broad component at the source velocity and the extremely broad component, respectively.

#### 4.5. Photodissociation of H<sub>2</sub>O

The ratio of the [O I] to H<sub>2</sub>O emission can constrain the velocity where H<sub>2</sub>O becomes dissociated. For example, in irradiated C-shock models, the O abundance decreases with shock velocity, while the H<sub>2</sub>O abundance increases, resulting in a decreasing [O I]/H<sub>2</sub>O ratio (Melnick & Kaufman 2015; Godard et al. 2019), the opposite to this SOFIA observation shows. A high UV radiation would promote photodissociation, efficiently destroying H<sub>2</sub>O; however, Lehmann et al. (2020) find only J-shocks can produce sufficient UV radiation to generate significant photodissociation. Smooth, steady-state disk winds can reproduce the Herschel H<sub>2</sub>O observations that trace outflows and contain little dust to block the UV radiation due from the accreting protostar (Yvart et al. 2016). Thus, the cavity shock component can be a C-type shock irradiated by an exceptional amount of UV radiation from sources other than the shock itself, a J-type shock that shows increasing O abundance with



**Table 3.** Estimated abundances of O, CO, and H<sub>2</sub>O

Scenario	$X(\text{O})/X(O_{\text{total}})$	$X(\text{CO})/X(O_{\text{total}})$	$X(\text{H}_2\text{O})/X(O_{\text{total}})$
Extended	$(6.9 \pm 2.4) \times 10^{-1}$	$(3.1 \pm 0.3) \times 10^{-1}$	$(2.1 \pm 1.0) \times 10^{-3}$
Unresolved	$(8.8 \pm 3.1) \times 10^{-1}$	$(1.2 \pm 0.1) \times 10^{-1}$	$(2.0 \pm 1.0) \times 10^{-4}$
	$X(\text{O})^a$	$X(\text{CO})^a$	$X(\text{H}_2\text{O})^a$
Extended	$(1.4 \pm 0.5) \times 10^{-4}$	$(6.2 \pm 0.6) \times 10^{-5}$	$(4.2 \pm 2.0) \times 10^{-7}$
Unresolved	$(1.7 \pm 0.6) \times 10^{-4}$	$(2.4 \pm 0.2) \times 10^{-5}$	$(4.0 \pm 2.0) \times 10^{-8}$

<sup>a</sup>The total volatile oxygen abundance to H ( $X(O_{\text{total}})$ ) is assumed as  $2 \times 10^{-4}$ .

velocities (Lehmann et al. 2020), or disk winds. In Figure 14, we show the [O I]/H<sub>2</sub>O intensity ratio as a function of velocity. The ratio has a minimum at  $\sim 9$  km s<sup>-1</sup>, a value of  $\sim 5$  at the source velocity, 6.2 km s<sup>-1</sup>, and then increases to  $\sim 60$  at  $-10$  km s<sup>-1</sup>.

Only the [O I] emission shows an extremely broad component, suggesting that the shocks are fully dissociative. The modeled column density of this component is  $(2.7 \pm 1.6) \times 10^{16}$  cm<sup>-2</sup>, assuming a kinetic temperature of 750 K. The models of FUV irradiated C-shocks break down at velocity  $\sim 20$  km s<sup>-1</sup>, assuming a pre-shock density of  $10^5$  cm<sup>-3</sup>, becoming dissociative at larger velocities (Melnick & Kaufman 2015). The lack of H<sub>2</sub>O emission beyond  $v \lesssim -15$  km s<sup>-1</sup> is consistent with its photodissociation in a J-type shock. Hollenbach (1985) presented a simple J-shock model, suggesting that [O I] emission dominates the cooling at  $T \lesssim 5000$  K. If we take  $T = 5000$  K as an upper limit of the [O I] temperature for the extremely broad component, we can estimate a lower limit of [O I] column density of  $2 \times 10^{16}$  cm<sup>-2</sup> from the non-LTE radiative transfer modeling (Figure 13).

#### 4.6. Mass Loss Rates

A longstanding issue with molecular outflows is whether they can be driven by stellar winds or jets. The basic idea is that the wind emerges from the star and/or disk at high speeds and sweeps out a cavity in the infalling core. The swept-up gas is observed in low rotational transitions of CO. The highly radiative nature of the shocks in the molecular gas imply that only the momentum of the wind is available to sweep up material (so-called ‘‘momentum conserving’’ situations). In this picture, the momentum in the CO flow must be matched by the momentum of the wind,

$$P_w = P_{\text{CO}} = M_w v_w = M_{\text{CO}} v_{\text{CO}} \quad (4)$$

If this is correct, an intrinsic mass loss rate in the wind can be derived from

$$\dot{M}_* = P_{\text{CO}} / (t_{\text{CO}} v_w) = F_{\text{CO}} / v_w, \quad (5)$$

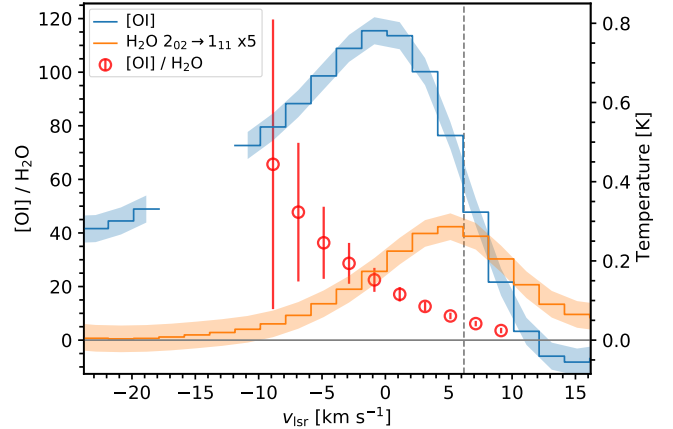


**Figure 14.** The ratio of [O I] 63  $\mu\text{m}$  and the H<sub>2</sub>O 2<sub>02</sub>  $\rightarrow$  1<sub>11</sub> line intensities as a function of velocity (red circles). The spectra of [O I] and H<sub>2</sub>O are smoothed to 2 km s<sup>-1</sup> before calculating the ratio. Only data with a  $> 1\sigma$  signal is included when calculating the ratio. The smoothed spectra of [O I] and H<sub>2</sub>O are shown (right axis) for comparison. The shaded region shows the uncertainties of the [O I] and H<sub>2</sub>O smooth spectra in their respective colors. The dashed vertical line indicates the source velocity, while the solid horizontal line highlights the baseline.

where  $F_{\text{CO}}$  is the average force that must have been applied to the swept-up gas,  $v_{\text{CO}}$  is the velocity of the swept-up gas, and  $v_w$  is the velocity of the stellar wind. The intrinsic mass loss rate is averaged over the age of the flow,  $t_{\text{CO}}$ . This basic idea was developed by Lévêque (1988) and applied to CO maps of young stellar objects, including L1551 IRS 5. Maps of CO are readily obtained, while observations of the wind itself have proved challenging. Since the latter inevitably average over much shorter times, comparison of the two provides a potential means to measure changes, whether secular or episodic, in the intrinsic mass loss rate ( $\dot{M}_*$ ), which in turn, is likely to be closely related to the mass accretion rate onto the star, a quantity of considerable interest. The binary protostars of L1551 IRS 5 drive two jets, as can be seen in [Fe II] (Fridlund & Liseau 1998; Pyo et al. 2009), but remain unresolved with [O I] and other trac-

ers. Thus, we are measuring the total intrinsic mass loss rate instead of rates for individual jets.

There have been many maps of different transitions of CO toward L1551 IRS 5, with a wide range of inferred momenta. For the most stringent test of the constancy of the mass loss rate, we prefer the largest, most complete maps of the lower  $J$  transitions of CO, which turn out to be the oldest. The outflow was the first bipolar flow discovered (Snell et al. 1980), but better maps were made in the  $J = 1 \rightarrow 0$  transition by Snell & Schloerb (1985) and the  $J = 2 \rightarrow 1$  transition by Levreault (1988) both covering about  $30'$ .

Determination of the force from the observations can take various paths, with issues of how to handle the fact that the outflow is inclined to the plane of sky ( $\theta_{\text{incl}}$ ). Some definitions of the inclination angle use the angle between the outflow axis and the plane of the sky, while others use the line of sight to the observer as the reference. We adopt the former. The L1551 IRS 5 outflow is mostly in the plane of the sky, and we adopt  $\theta_{\text{incl}} = 30^\circ$ , based on a determination of the disk angle ( $90 - \theta_{\text{incl}}$ ) of  $60^\circ \pm 5^\circ$  (Chou et al. 2014).

Following Dunham et al. (2014), we make no correction to the observed  $P_{\text{CO}}$  (see also Downes & Cabrit 2007) but correct  $t_{\text{CO}}$  because both length and velocity are affected. For our convention on inclination angle,

$$t_{\text{CO}} = t_{\text{obs}} \times \tan(\theta_{\text{incl}}). \quad (6)$$

This approach is similar to Method M7 of van der Marel et al. (2013). Therefore, forces determined from observations, with no corrections, should be multiplied by  $1/\tan(\theta_{\text{incl}}) = 1.73$ . We added forces for the blue and red lobes. The result for the  $J = 1 \rightarrow 0$  map of Snell & Schloerb (1985), after correction of age by inclination angle, is  $F_{\text{CO}} = 1.2 \times 10^{-4} M_\odot \text{ yr}^{-1} \text{ km s}^{-1}$  averaged over an age of  $4.6 \times 10^4$  yr. The result from the  $J = 2 \rightarrow 1$  map from Levreault (1988), is  $F_{\text{CO}} = 2.1 \times 10^{-4} M_\odot \text{ yr}^{-1} \text{ km s}^{-1}$  averaged over an age of  $2.9 \times 10^4$  yr corrected by inclination angle.

The wind velocity has been estimated from spectra of [Fe II]  $\lambda = 1.644 \mu\text{m}$  emission. Pyo et al. (2005) find velocities as high as  $300 \text{ km s}^{-1}$ , with a blue-shifted components at  $100 \text{ km s}^{-1}$  to  $279 \pm 10 \text{ km s}^{-1}$ . Giovanardi et al. (1992) also observed velocities up to  $150 \text{ km s}^{-1}$  in HI. Correcting for inclination by  $1/\sin(\theta_{\text{incl}}) = 2$  implies  $v_w = 200$  to  $560 \text{ km s}^{-1}$  for ionized gas and  $v_w = 260 \text{ km s}^{-1}$  for the neutral gas. Such high velocities strongly indicate an origin for the wind near the star, rather than a disk wind. The SOFIA [O I] observations only detect [O I] up to  $\sim 75 \text{ km s}^{-1}$  in blue-shift, which may be due to insufficient sensitivity. We used  $v_w = 300 \text{ km s}^{-1}$  as a compromise. The values for  $\dot{M}_*$  are then  $4.0 \times 10^{-7}$

$M_\odot \text{ yr}^{-1}$  for  $J = 1 \rightarrow 0$  and  $7.0 \times 10^{-7} M_\odot \text{ yr}^{-1}$  for  $J = 2 \rightarrow 1$ .

Yıldız et al. (2015) also mapped the outflow of L1551 IRS 5 using the CO  $J = 3 \rightarrow 2$  line to derive the force and dynamical age of the blue- and red-shifted lobes; however, the map size is only  $\sim 5' \times 5'$ . We use their Equation 4 to retrieve the momentum without any correction,  $0.11$  and  $0.40 M_\odot \text{ km s}^{-1}$ , for the blue- and red-shifted outflow, respectively. They also measured a dynamical age of  $8.3 \times 10^3$  and  $6.7 \times 10^3$  yr uncorrected for inclination in the blue- and red-shifted outflow, respectively. Using Equation 5 to correct the averaged age for inclination angle, and  $v_w = 300 \text{ km s}^{-1}$ , we derive an intrinsic mass loss rate of  $4.0 \times 10^{-7} M_\odot \text{ yr}^{-1}$ , consistent with the estimates from low- $J$  CO emission.

In the momentum-conserving scenario, atomic winds are thought to drive the molecular outflows because the ionized wind/jet has too little momentum (Mundt et al. 1987). Giovanardi et al. (1992) observed the high velocity wings of HI line profiles using the Arecibo Observatory. Assuming optically thin emission and mass conservation of HI, they modeled the line profiles with a decelerating wind model to get  $\dot{M}_* = 2.4 \times 10^{-6} M_\odot \text{ yr}^{-1}$ . However, their model assumes that all HI gas is due to the wind, while photodissociation in the envelope can produce HI. Moreover, the HI spectra suffer from intervening structured clouds at the blue-shifted velocity. Thus, our SOFIA [O I] observations would better measure  $\dot{M}_*$  in atomic winds and so, in the following discussion, we focus on the extremely broad component of [O I].

[O I] is a good tracer of atomic outflows in the model proposed by Hollenbach (1985). The model has a fast ( $v_w$ ) wind from the star-disk system driving a shock into the infalling molecular gas, pushing it away from the forming star at speeds of a few to tens of  $\text{km s}^{-1}$  ( $v_m$ ). The slowing of the wind in the molecular shock then drives a reverse shock into the wind at  $v_{\text{wsh}} = v_w - v_m \sim v_w \text{ km s}^{-1}$ . In this model, the molecular shock is formed in the ambient material, producing the emission from CO, H<sub>2</sub>, H<sub>2</sub>O, and OH. The rapid deceleration of the wind as it encounters the molecular material produces the wind shocks, resulting in a J-type shocked region, with  $T_K = 10^3 - 10^5$  K. Such a high temperature would dissociate most molecules, making the fine-structure [O I]  $63 \mu\text{m}$  line the dominant coolant in the shocked wind. The shocks are strongly radiative and only the momentum of the wind is assumed to be available to accelerate the molecular outflow. Thus, in this model, [O I]  $63 \mu\text{m}$  emission can conveniently be related to the intrinsic mass loss rate by Hollenbach (1985)

$$\frac{L_{[\text{OI}] 63 \mu\text{m}}}{L_{\odot}} = \frac{0.1 \dot{M}_{\star}}{10^{-5} M_{\odot} \text{yr}^{-1}}. \quad (7)$$

Using the flux of the extremely broad [O I] component that traces high-velocity gas (Table 2), we can derive  $\dot{M}_{\star} = 3.4 \pm 1.8 \times 10^{-7} M_{\odot} \text{yr}^{-1}$  using the observed [O I] luminosity,  $3.4 \pm 1.8 \times 10^{-3} L_{\odot}$ , assuming that the missing red-shifted [O I] emission has the same luminosity as the observed blue-shifted part. If we adopt the total [O I] 63  $\mu\text{m}$  luminosity from Herschel observations,  $4.8 \pm 0.1 \times 10^{-3} L_{\odot}$  (Green et al. 2016),  $\dot{M}_{\star}$  becomes  $4.8 \pm 0.1 \times 10^{-7} M_{\odot} \text{yr}^{-1}$ . Sperling et al. (2021) also estimated  $\dot{M}_{\star}$  using the [O I] emission observed with SOFIA/FIFI-LS. They employed two methods, one assuming collisionally excited [O I] emission from purely atomic oxygen gas (Sperling et al. 2020) and the other one using the relation in Hollenbach (1985), deriving  $\dot{M}_{\star}$  of  $5.8\text{--}11.8 \times 10^{-7}$  and  $4.9\text{--}5.4 \times 10^{-7} M_{\odot} \text{yr}^{-1}$ , respectively.

Equation 7 provides a zeroth-order estimate of the intrinsic mass loss rate and there are important caveats. This method assumes the entire wind shock radiates before any gas gets shock-heated or entrained, which only occurs when measuring the jet close to its source (Hartigan et al. 2019). Secondly, if the observations probe several unresolved shocks instead of a single shock, Equation 7 may overestimate the intrinsic mass loss rate (Nisini et al. 2015). Finally, if parts of the wind propagate without intervention, this method would underestimate the intrinsic mass loss rate (Cohen et al. 1988). With the velocity-resolved SOFIA [O I] observations, we can directly estimate the mass outflow rate traced by [O I] to partially circumvent these caveats, especially the first one. If the extremely broad component of [O I] traces the atomic wind that carries most momentum in the wind, we can simply estimate  $\dot{M}_{\star}$  by taking the ratio of the mass traced by [O I] and the dynamical time. With a column density of  $2.7 \pm 1.6 \times 10^{16} \text{cm}^{-2}$ , we can estimate the mass outflow rate using

$$\begin{aligned} \dot{M}_{\star} &= \frac{\mu m_{\text{H}} N_{[\text{OI}]} \Omega_{\text{b}} / X_{\text{O}}}{t_{\text{dyn}}}; \\ t_{\text{dyn}} &= \frac{R_{\text{beam}}}{v_{[\text{OI}]}} \tan(\theta_{\text{incl}}), \end{aligned} \quad (8)$$

where  $\mu$  is the mean molecular weight of 2.8 (Kauffmann et al. 2008),  $\Omega_{\text{b}}$  ( $1.13 \times 6''^2$ ) is the area of the Gaussian beam with FWHM =  $6''.3$ ,  $X_{\text{O}}$  is the atomic oxygen abundance,  $t_{\text{dyn}}$  is the inclination-corrected dynamical time of the [O I] gas,  $R_{\text{beam}}$  is the radius of the beam, and  $v_{[\text{OI}]}$  is the velocity of [O I] gas. We estimate the dynamical age of the wind as the time required for the gas to cross the beam radius with correction of inclination

angle. The  $t_{\text{dyn}}$  is 35 yr. The atomic oxygen abundance is a key parameter to relate the [O I] mass flux to the intrinsic mass outflow rate. Because neither the  $\text{H}_2\text{O}$  nor high- $J$  CO emission shows an extremely broad component, this component is likely to be fully dissociated. Thus, if we assume a total oxygen volatile abundance ( $X_{\text{O}}$ ),  $3.4 \times 10^{-4}$ , as discussed in Section 4.4, and an equal rate in each outflow lobe, the intrinsic mass outflow rate becomes  $1.3 \pm 0.8 \times 10^{-6} M_{\odot} \text{yr}^{-1}$ . Considering the uncertainty, the intrinsic mass outflow rate from [O I] agrees with not only the estimate from HI but also our estimate from the CO outflows after inclination correction, unambiguously confirming the momentum-driven outflows. In this scenario, both atomic and ionized wind belongs to the mass ejected near from the protostar but the atomic wind carries most of the momentum, driving the molecular outflows. Given its spectral profile in the optical and near-infrared, some studies consider L1551 IRS 5 as a FU Orionis-like object (e.g., Mundt et al. 1985; Connelley & Greene 2010), which implies it should have a strongly varying time-dependent mass loss rate. But the similar  $\dot{M}_{\star}$  found over a  $3\text{--}5 \times 10^4$  yr (low- $J$  CO) and 35 yr ([O I]) timescales suggests no evidence of varying  $\dot{M}_{\star}$  within a factor of 3.

## 5. CONCLUSIONS

This work presents SOFIA/upGREAT observations of [O I] and [C II] emission toward a Class I protostar, L1551 IRS 5. The main conclusions are listed below.

- The SOFIA/upGREAT observations show an asymmetric profile for the [O I] 63  $\mu\text{m}$  line toward the center of L1551 IRS 5. Emission of [O I] only appears in the blue-shifted velocity with a FWHM of  $\sim 100 \text{km s}^{-1}$ . A two-component model can reproduce this [O I] spectrum, indicating a  $\sim 20 \text{km s}^{-1}$  width component at the source velocity and another extremely wide component,  $87.5 \text{km s}^{-1}$ , at  $-30 \text{km s}^{-1}$ .
- The [O I] line profile is consistent with the scenario of cavity shocks and spot shocks due to the outflow-envelope interaction. The [O I] component centered at the source velocity appears similar to the line profiles of high- $J$  CO and  $\text{H}_2\text{O}$  lines, which have a  $\sim 20 \text{km s}^{-1}$  component around the source velocity tracing the cavity shocks. Spot shocks would produce a line profile similar to the velocity-offset extremely broad [O I] component. This extremely broad component is only detected in [O I] emission. The non-detection of a narrow ( $< 5 \text{km s}^{-1}$ ) [O I] component suggests that shocked gas dominates the [O I] emission.

- Narrow [C II] emission is detected at the protostar and in the red-shifted outflow with a S/N of 4.1 and 3.4, and line widths of 2.3 and 2.8 km s<sup>-1</sup>, respectively. The narrow line width suggests a PDR origin for the [C II] emission. Comparing to the Herschel observations, we estimate the PDR contribution to [O I] and [C II] line flux is ~3% and ~30%, respectively.
- We use non-LTE radiative transfer calculations to derive the column densities of [O I], CO, and H<sub>2</sub>O in the component tracing the cavity shocks. We consider the scenarios that the emission is uniformly extended and unresolved. The atomic oxygen abundance is 69±24% and 88±31% of the total oxygen volatile abundance in L1551 IRS 5 for the extended and unresolved scenarios, respectively. Assuming an observable oxygen abundance of  $3.4 \times 10^{-4}$  and a refractory dust abundance of  $1.4 \times 10^{-4}$ , we estimate an atomic oxygen abundance of  $1.4 \pm 0.5 \times 10^{-4}$  and  $1.7 \pm 0.6 \times 10^{-4}$  with respect to atomic H for the extended and unresolved cases, respectively, indicating that the emission originates in atomic cavity shocks.
- The intrinsic mass loss rate ( $\dot{M}_*$ ) derived from [O I] component is  $1.3 \pm 0.8 \times 10^{-6} M_\odot \text{ yr}^{-1}$ . Observations of CO outflows, HI wind, and [O I] wind produce consistent values of  $\dot{M}_*$ , unambiguously confirming the momentum-conserving scenario of outflows. There is no evidence of varying  $\dot{M}_*$  over  $3\text{--}5 \times 10^4 \text{ yr}$  to a factor of 3.

These SOFIA/upGREAT observations suggest a highly atomic outflow in L1551 IRS 5, opposite to the conclusions of previous [O I] observations in the outflow of low-mass protostars (Kristensen et al. 2017a). With velocity-resolved spectra, we can directly identify components of shocked gas and investigate their physical origin. Future observations with high sensitivity can reduce the uncertainties presented in this study. Moreover, velocity-resolved [O I] emission has only previously

been observed toward two protostellar outflows. Thus, a full picture of the outflow-envelope interaction requires future studies on the shocked gas in outflows as well as more [O I] observations in outflows.

The authors thank Edward Chambers and Simon Coudé for the observing support. Y.-L. Yang acknowledges the support from the Virginia Initiative of Cosmic Origins (VICO) Postdoctoral Fellowship. Y.-L. Yang also appreciates discussions with Fernando Cruz-Saenz de Miera, Ágnes Kóspál, Michihiro Takami, and Ilse Cleeves. This study is based on observations made with the NASA/DLR Stratospheric Observatory for Infrared Astronomy (SOFIA). SOFIA is jointly operated by the Universities Space Research Association, Inc. (USRA), under NASA contract NNA17BF53C, and the Deutsches SOFIA Institut (DSI) under DLR contract 50 OK 0901 to the University of Stuttgart. Financial support for this work was provided by NASA through award #NAS2-97001, SOF 04-0146 and 06-0104, issued by USRA. A.K. acknowledges support from the First TEAM grant of the Foundation for Polish Science No. POIR.04.04.00-00-5D21/18-00. This article has been supported by the Polish National Agency for Academic Exchange under Grant No. PPI/APM/2018/1/00036/U/001. J.P.R. acknowledges support from the Virginia Initiative on Cosmic Origins (VICO), the National Science Foundation (NSF) under grant nos. AST-1910106 and AST-1910675, and NASA via the Astrophysics Theory Program under grant no. 80NSSC20K0533. Herschel is an ESA space observatory with science instruments provided by European-led Principal Investigator consortia and with important participation from NASA.

*Facilities:* SOFIA

*Software:* Class v. sep20a (Gildas Team 2013), Astropy v. 4.2 (Astropy Collaboration et al. 2013, 2018), Matplotlib v. 3.3.4 (Hunter 2007), JupyterLab v. 3.0.16 (Kluyver et al. 2016)

## REFERENCES

- Astropy Collaboration, Robitaille, T. P., Tollerud, E. J., et al. 2013, *A&A*, 558, A33
- Astropy Collaboration, Price-Whelan, A. M., Sipőcz, B. M., et al. 2018, *AJ*, 156, 123
- Bjerkeli, P., van der Wiel, M. H. D., Harsono, D., Ramsey, J. P., & Jørgensen, J. K. 2016, *Nature*, 540, 406
- Chou, T.-L., Takakuwa, S., Yen, H.-W., Ohashi, N., & Ho, P. T. P. 2014, *ApJ*, 796, 70
- Codella, C., Bachiller, R., & Reipurth, B. 1999, *A&A*, 343, 585
- Cohen, M., Hollenbach, D. J., Haas, M. R., & Erickson, E. F. 1988, *ApJ*, 329, 863
- Connelley, M. S., & Greene, T. P. 2010, *AJ*, 140, 1214
- Cruz-Sáenz de Miera, F., Kóspál, Á., Ábrahám, P., Liu, H. B., & Takami, M. 2019, *ApJL*, 882, L4
- Downes, T. P., & Cabrit, S. 2007, *A&A*, 471, 873



- Draine, B. 2010, *Physics of the Interstellar and Intergalactic Medium*, Princeton Series in Astrophysics (Princeton University Press).  
<https://books.google.com/books?id=FycJvKHYiwsC>
- Dunham, M. M., Arce, H. G., Mardones, D., et al. 2014, *ApJ*, 783, 29
- Ercolano, B., & Owen, J. E. 2016, *MNRAS*, 460, 3472
- Fridlund, C. V. M., Bergman, P., White, G. J., Pilbratt, G. L., & Tauber, J. A. 2002, *A&A*, 382, 573
- Fridlund, C. V. M., & Liseau, R. 1998, *ApJL*, 499, L75
- Galli, P. A. B., Loinard, L., Ortiz-Léon, G. N., et al. 2018, *ApJ*, 859, 33
- Gildas Team. 2013, *GILDAS: Grenoble Image and Line Data Analysis Software*, , ascl:1305.010
- Giovanardi, C., Lizano, S., Natta, A., Evans, Neal J., I., & Heiles, C. 1992, *ApJ*, 397, 214
- Godard, B., Pineau des Forêts, G., Lesaffre, P., et al. 2019, *A&A*, 622, A100
- Green, J. D., Yang, Y.-L., Evans, Neal J., I., et al. 2016, *AJ*, 151, 75
- Gressel, O., Ramsey, J. P., Brinch, C., et al. 2020, *ApJ*, 896, 126
- Gusdorf, A., Anderl, S., Lefloch, B., et al. 2017, *A&A*, 602, A8
- Hartigan, P., Holcomb, R., & Frank, A. 2019, *ApJ*, 876, 147
- Hayashi, M., & Pyo, T.-S. 2009, *ApJ*, 694, 582
- Hollenbach, D. 1985, *Icarus*, 61, 36
- Hollenbach, D., & McKee, C. F. 1989, *ApJ*, 342, 306
- Hollenbach, D. J., & Tielens, A. G. G. M. 1999, *Reviews of Modern Physics*, 71, 173
- Hunter, J. D. 2007, *Computing in Science & Engineering*, 9, 90
- Karska, A., Kristensen, L. E., van Dishoeck, E. F., et al. 2014a, *A&A*, 572, A9
- Karska, A., Herpin, F., Bruderer, S., et al. 2014b, *A&A*, 562, A45
- Karska, A., Kaufman, M. J., Kristensen, L. E., et al. 2018, *ApJS*, 235, 30
- Kauffmann, J., Bertoldi, F., Bourke, T. L., Evans, N. J., I., & Lee, C. W. 2008, *A&A*, 487, 993
- Kaufman, M. J., Wolfire, M. G., Hollenbach, D. J., & Luhman, M. L. 1999, *ApJ*, 527, 795
- Kluyver, T., Ragan-Kelley, B., Pérez, F., et al. 2016, in *Positioning and Power in Academic Publishing: Players, Agents and Agendas*, ed. F. Loizides & B. Schmidt, IOS Press, 87 – 90
- Kristensen, L. E., Gusdorf, A., Mottram, J. C., et al. 2017a, *A&A*, 601, L4
- Kristensen, L. E., van Dishoeck, E. F., Bergin, E. A., et al. 2012, *A&A*, 542, A8
- Kristensen, L. E., van Dishoeck, E. F., Mottram, J. C., et al. 2017b, *A&A*, 605, A93
- Lee, J.-E., Lee, J., Lee, S., Evans, Neal J., I., & Green, J. D. 2014, *ApJS*, 214, 21
- Lehmann, A., Godard, B., Pineau des Forêts, G., & Falgarone, E. 2020, *A&A*, 643, A101
- Leurini, S., Wyrowski, F., Wiesemeyer, H., et al. 2015, *A&A*, 584, A70
- Levreault, R. M. 1988, *ApJS*, 67, 283
- Lim, J., & Takakuwa, S. 2006, *ApJ*, 653, 425
- Lim, J., Yeung, P. K. H., Hanawa, T., et al. 2016, *ApJ*, 826, 153
- Lupton, R., Blanton, M. R., Fekete, G., et al. 2004, *PASP*, 116, 133
- Melnick, G. J., & Kaufman, M. J. 2015, *ApJ*, 806, 227
- Mottram, J. C., Kristensen, L. E., van Dishoeck, E. F., et al. 2014, *A&A*, 572, A21
- Mottram, J. C., van Dishoeck, E. F., Kristensen, L. E., et al. 2017, *A&A*, 600, A99
- Mundt, R., Brugel, E. W., & Buehrke, T. 1987, *ApJ*, 319, 275
- Mundt, R., Stocke, J., Strom, S. E., Strom, K. M., & Anderson, E. R. 1985, *ApJL*, 297, L41
- Nisini, B., Santangelo, G., Giannini, T., et al. 2015, *ApJ*, 801, 121
- Ossenkopf, V., & Henning, T. 1994, *A&A*, 291, 943
- Pequignot, D. 1990, *A&A*, 231, 499
- Przybilla, N., Nieva, M.-F., & Butler, K. 2008, *ApJL*, 688, L103
- Pyo, T.-S., Hayashi, M., Kobayashi, N., Terada, H., & Tokunaga, A. T. 2009, *ApJ*, 694, 654
- Pyo, T.-S., Hayashi, M., Kobayashi, N., et al. 2005, *ApJ*, 618, 817
- Risacher, C., Güsten, R., Stutzki, J., et al. 2016, *A&A*, 595, A34
- . 2018, *Journal of Astronomical Instrumentation*, 7, 1840014
- Riviere-Marichalar, P., Merín, B., Kamp, I., Eiroa, C., & Montesinos, B. 2016, *A&A*, 594, A59
- Rodríguez, L. F., Porras, A., Claussen, M. J., et al. 2003, *ApJL*, 586, L137
- Rodríguez, L. F., D'Alessio, P., Wilner, D. J., et al. 1998, *Nature*, 395, 355
- Schneider, N., Röllig, M., Simon, R., et al. 2018, *A&A*, 617, A45
- Schneider, N., Röllig, M., Polehampton, E. T., et al. 2021, *A&A*, 653, A108
- Schöier, F. L., van der Tak, F. F. S., van Dishoeck, E. F., & Black, J. H. 2005, *A&A*, 432, 369



- Skrutskie, M. F., Cutri, R. M., Stiening, R., et al. 2006, *AJ*, 131, 1163
- Snell, R. L., Loren, R. B., & Plambeck, R. L. 1980, *ApJL*, 239, L17
- Snell, R. L., & Schloerb, F. P. 1985, *ApJ*, 295, 490
- Sofia, U. J., Lauroesch, J. T., Meyer, D. M., & Cartledge, S. I. B. 2004, *ApJ*, 605, 272
- Sperling, T., Eislöffel, J., Fischer, C., et al. 2020, *A&A*, 642, A216
- . 2021, *A&A*, 650, A173
- Takakuwa, S., Saigo, K., Matsumoto, T., et al. 2020, *ApJ*, 898, 10
- Temi, P., Hoffman, D., Ennico, K., & Le, J. 2018, *Journal of Astronomical Instrumentation*, 07, 1840011.  
<https://doi.org/10.1142/S2251171718400111>
- Tielens, A. G. G. M., & Hollenbach, D. 1985, *ApJ*, 291, 722
- van der Marel, N., Kristensen, L. E., Visser, R., et al. 2013, *A&A*, 556, A76
- van der Tak, F. F. S., Black, J. H., Schöier, F. L., Jansen, D. J., & van Dishoeck, E. F. 2007, *A&A*, 468, 627
- van Dishoeck, E. F., Kristensen, L. E., Mottram, J. C., et al. 2021, *A&A*, 648, A24
- van Kempen, T. A., Kristensen, L. E., Herczeg, G. J., et al. 2010, *A&A*, 518, L121
- White, R. J., & Hillenbrand, L. A. 2004, *ApJ*, 616, 998
- Wu, P.-F., Takakuwa, S., & Lim, J. 2009, *ApJ*, 698, 184
- Yang, Y.-L., Green, J. D., Evans, Neal J., I., et al. 2018, *ApJ*, 860, 174
- Yıldız, U. A., Kristensen, L. E., van Dishoeck, E. F., et al. 2013, *A&A*, 556, A89
- . 2015, *A&A*, 576, A109
- Yvart, W., Cabrit, S., Pineau des Forêts, G., & Ferreira, J. 2016, *A&A*, 585, A74